CO_2-Based Leaching of Sulfidic Peridotite Drives Critical Mineral Mobilization and Carbonate Precipitation

Madeline A. Murchland [a†]*, Quin R.S. Miller [a]*, Alexandra B. Nagurney [a], C. Heath Stanfield [a], Nabajit Lahiri [a], Joshua A. Silverstein [a], Yuntian Teng [a], Emily T. Nienhuis [b], Mark H. Engelhard [a], Connor Mulcahy [c], H. Todd Schaef [a]

[a] Energy and Environment Directorate, Pacific Northwest National Laboratory, Richland, Washington, USA
[b] Physical and Computational Sciences Directorate, Pacific Northwest National Laboratory, Richland, Washington, USA
[c] Division of Environmental Management, Wisconsin Department of Natural Resources, Milwaukee, Wisconsin, USA
[†] Current affiliation is Department of Geology and Geological Engineering, Colorado School of Mines, Golden, Colorado, USA

KEYWORDS: carbon dioxide removal, critical materials, geologic carbon sequestration, carbon mineralization, critical minerals, nickel

ABSTRACT: The transition towards green energy requires both carbon dioxide removal and consistent supplies of energy-critical minerals. Injection and mineralization of supercritical CO_2 at active mafic and ultramafic-hosted mines provides a potential avenue to achieve both, through the stable geologic storage of carbon and subsequent mobilization of critical metals. A sample from the Eagle occurrence, an ultramafic-hosted sulfide deposit in Michigan, USA that is the only active Ni mine in the United States, was characterized both before and after reaction with supercritical CO_2 at elevated pressure and temperature. We present the changes in mineralogy, feature relocation, and potential for carbon mineralization and critical mineral recovery based on the comparison of pre- and post-reaction datasets. Herein, we present evidence of dissolution-precipitation reactions leading to carbon mineralization and critical mineral mobilization driven by water-saturated supercritical CO_2 fluids, including the formation of aragonite and dissolution-reprecipitation of Ni phases Collectively, these results will improve fate and transport models for carbon storage in ultramafic rocks, increase understanding of new unconventional sources for critical minerals, and provide a foundation for future studies on CO_2 enhanced mineral recovery (CO_2-EMR).

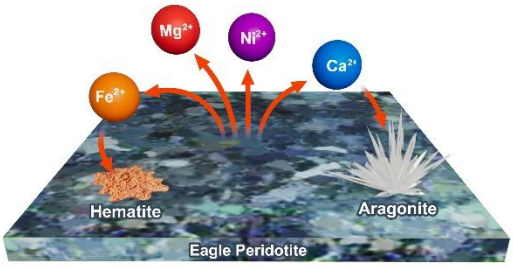

Synopsis: This experimental study highlights critical minerals mobilization coupled with permanent carbon storage with rocks from the only active nickel mine in the United States.

INTRODUCTION

Carbon capture and storage (CCS) is foundational to current climate mitigation strategies[1]. Geological storage is a well-studied CCS approach that sequesters carbon emissions into stable carbonate minerals; *in situ* geological storage, or mineral carbonation, has been successful in both laboratory experiments and at the field-scale.[2, 3-6] In this approach, anthropogenic emissions are injected directly into a host rock containing reactive silicates, which provide divalent metal cations to form carbonate minerals. Mafic (i.e. basalt) and ultramafic (i.e. peridotite) lithologies generally contain abundant divalent magnesium, calcium, and iron bound in silicates such as olivine, and are therefore considered excellent host formations for carbon storage via mineralization.[7, 8, 9]

Peridotite carbonation behavior has been extensively studied in the context of natural processes, mine tailings, and anthropogenic carbon mineralization in the subsurface.[7, 10, 11, 12] Peridotites are predominantly composed of olivine with abundant pyroxene, and typically contain Ca-rich plagioclase feldspar. Olivine has been aggressively studied in the context of carbon mineralization due to its prevalence, simple chemistry, and rapid carbonation kinetics.[13, 14] Olivine dissolution (c.f.[15]) and carbonation[11, 13, 16, 17, 18] behavior, including reactivity in water-bearing supercritical carbon dioxide ($scCO_2$) fluids,[3, 13, 14, 17, 19, 20] is well-documented, as is the dissolution[21] and carbonation[18, 20, 22, 23] behavior of pyroxene. Plagioclase feldspar dissolution[24] is also well understood, though its carbonation[25] behavior is relatively understudied compared to olivine, pyroxene, or peridotite more generally.

The process of mineral carbonation in peridotites has also been shown to mobilize trace metals in the host rock, largely from the dissolution of olivine[26, 27, 28]. This has important implications for ultramafic lithologies, which are well documented to be

associated with sulfide deposits and are commonly enriched in Ni, Cu, Cr, and platinum-group elements (PGEs).[29, 30] These elements are among those known as energy-critical minerals, designated as such because they are essential to several kinds of existing and emerging technologies, such as those in the green, AI, and aerospace sectors, yet have unstable or depleted supplies. Specifically, Ni is essential in many energy storage batteries and will continue to be a necessary commodity in the wind, solar, nuclear, geothermal, and carbon capture technology fields.[31, 32] Exploitable quantities of these critical minerals occur in ultramafic mines worldwide as sulfide and oxide deposits, with over 150 defined resources of Cu-Ni-PGE sulfides and over 120 of magmatic oxides.[29] However, the prevalence of these energy-relevant resources, specifically Ni and Co, in the olivine structure[33] coupled with the volume of olivine in the gangue and host rock of these deposits, has spurred on the burgeoning research fields of coupling critical mineral recovery with carbon storage in subsurface and subaerial environments that this study contributes to.[5, 6, 9, 12, 26, 27, 34, 35, 36]

Herein, we examined the carbonation and critical mineral mobilization for sulfidic peridotite exposed to supercritical CO_2 fluids, strategically choosing a sample from the only active Ni mine in the United States. The Eagle and Eagle East intrusions, which host this Ni mine, are two mafic-ultramafic intrusions situated about 40 kilometers northwest of Marquette, Michigan, USA. Emplaced into Paleoproterozoic black slates, both intrusions are sub-vertical and roughly funnel shaped. They are petrogenetically associated with the early stages of the 1.1 Ga Midcontinent Rift, which is a large igneous province exposed in the Lake Superior region. Both intrusions host economic Ni-Cu-PGE magmatic sulfide mineralization[37] and have been actively mined by the Lundin Mining Corporation since 2014. The dominant silicate minerals in both intrusions are olivine, pyroxene, and plagioclase, while dominant sulfides include pentlandite (Ni-Fe), millerite (Ni), violarite (Ni-Fe), chalcopyrite (Cu-Fe), cubanite (Cu-Fe), and pyrrhotite (Fe). Sulfide minerals make up at least 1-3% of the rock volume in any given portion of both intrusions, and in significant fractions of both intrusions, sulfide minerals make up from 25% to nearly 100% of the rock volume.[38] Traditional mining methods at the Eagle deposit primarily target pentlandite and chalcopyrite.

The goal of this study was to determine reaction outcomes with respect to critical mineral mobilization from olivine and permanent carbon storage via carbonate mineralization in an experimental system that simulates the use of hydrated CO_2 as a leaching fluid. In this work, we reacted an olivine and sulfide-bearing rock chip from the Eagle Intrusion with a water-saturated, CO_2-dominant fluid at elevated

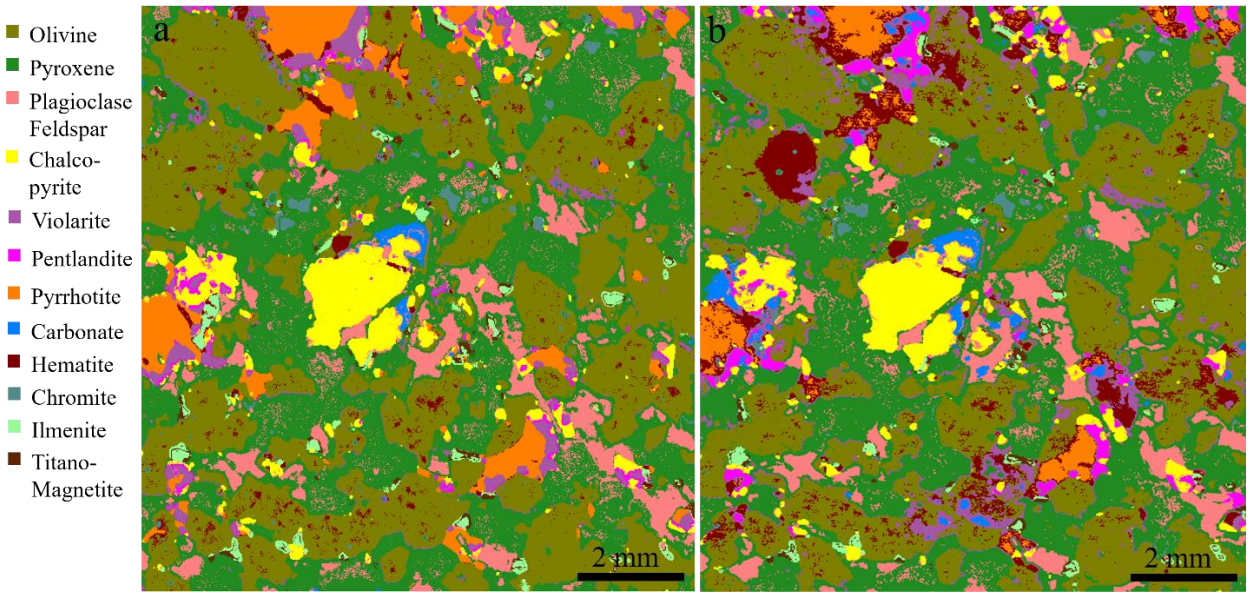

Figure 1. False color mineral maps of the a) unreacted and b) reacted Eagle rock chip. Carbonation-driven dissolution-precipitation reactions are evidenced by the change in distribution and amount of carbonate, hematite, and sulfides. A quantitative comparison of phase distribution can be found in Table S1.

pressure and temperature in pressure vessel reactors for several weeks. By combining feature-relocation imaging, compositional analysis, and spectroscopy to compare the sample before and after reaction, we gained insights into the critical mineral transformations that occur during carbon mineralization. This characterization of trace metal mobility during simulated in situ mineral carbonation increases the overall understanding required to implement CCS. Coupling the concepts of carbon storage and critical mineral transport will provide additional carbon storage incentives at active mines and related ultramafic targets, forging pathways towards carbon-neutral and carbon-negative mining strategies and positioning gangue and host rock as potential resources

METHODS AND MATERIALS

Eagle Intrusion Peridotite Sample. This study focused on a ~13×12×4mm chip of peridotite from the Eagle Intrusion. The sample was characterized prior to reaction with a variety of microscopy techniques and micro-X-ray diffraction (µXRD). These methods revealed the chip to be composed predominantly of olivine and pyroxene, with additional plagioclase and Fe-, Cu-, and Ni-bearing sulfides, namely pentlandite, violarite, chalcopyrite, and pyrrhotite (**Figure 1**) which is consistent with the previously-described mineralogy of the sulfide-bearing lithologies at the Eagle Mine[38]. µXRF paired with AIMICS determined that the olivine composed 38.6% of the sample and averaged 3200 ppm Ni; this concentration is consistent with other analyses of Eagle deposit olivine[39]. This sample does not represent the high-grade lithology that is targeted with traditional mining, but rather is largely composed of reactive gangue and host rock silicates that can be targeted for metal cation release with carbonation-driven dissolution.

Micro X-ray Diffraction (µXRD). In situ spatially-resolved X-ray diffraction analysis was conducted on the post-reaction rock chip with our Bruker D8 Discover TXS-HE XRD system.[23, 40] The Eagle sample was mounted on the xyzϕχ stage and positioned using a laser-video alignment system. The XRD is contained in the A25 cabinet and equipped with a rotating Cu anode (Kα λ=1.5418 Å), 0.3x3 mm cassette tungsten filament, Atlas goniometer, and a UMC 1516 motorized stage. The power settings of the generator were 45 kV and 120 mA and the source-sample distance fixed at 425 mm. The EIGER2 R 500K detector was used in 2D mode and positioned at a 206.8 mm sample-detector distance. The ≤2 mm point beam was generated using a Montel mirror optic and various collimators.

Scanning Electron Microscopy and Energy Dispersive Spectroscopy (SEM-EDS). The imaging and analysis for investigating particle morphology was performed using a JEOL 7001F TTLS/LV instrument (JEOL USA, Inc.) scanning electron microscopy (SEM) configured with a field emission gun capable of imaging uncoated, non-conductive specimens in low vacuum mode. The SEM is equipped with a 60 mm^2 silicon drift detector (SDD) energy dispersive X-ray spectrometer (EDS; Bruker Quantax 6|60; Bruker Nano GmbH) used to determine the elements present in specimen areas of interest. Imaging and elemental analysis was performed using low vacuum

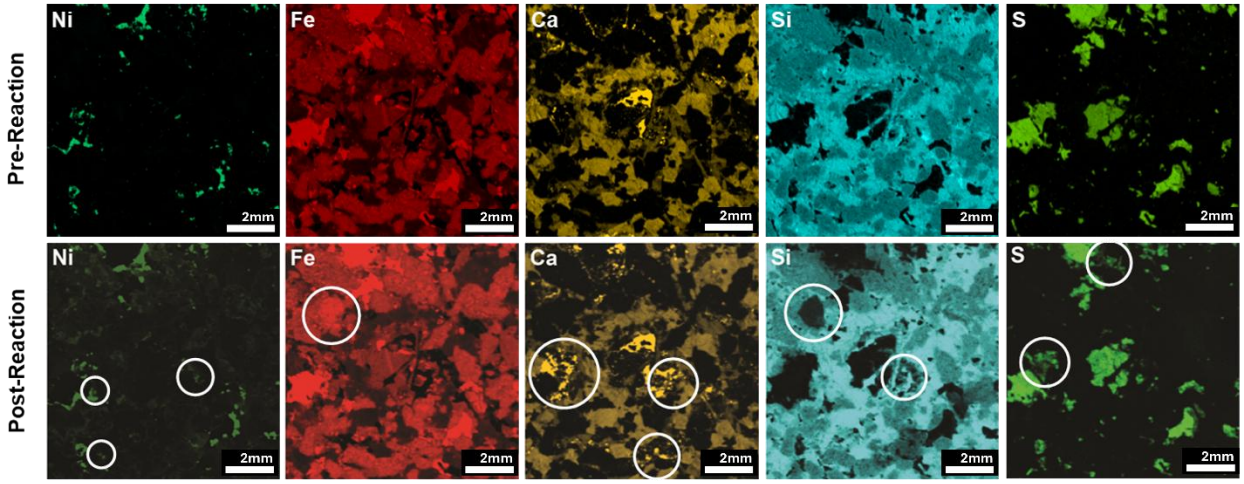

Figure 2. µ-XRF false color element maps of the peridotite chip, before and after reaction with water-saturated scCO2. Maps are labelled by element, and the top row shows the pre-reaction surface while the bottom row shows the same surface post-reaction. Circled areas indicate sites of clear mineral dissolution and precipitation in the post-reaction maps. Post-reaction maps of Ni, Fe, and Ca show new areas of metal precipitate, while Si and S maps indicate areas of reactivity and coverage by precipitates.

backscatter imaging mode at 15kV accelerating voltage and a probe current of ~0.3nA. Elemental maps were generated on select areas of interest for 300s with a count rate of ~50kcps. Composition maps and point spectra were collected using Bruker Esprit 2.3 software. Scanning electron microscopy and energy dispersive X-ray spectroscopy (SEM-EDS) results were used to characterize the mineralogy before and after carbonation, as well as to observe changes in carbonate minerals, trace metal phases, and olivine compositions. Secondary electron mode (SE) was also used to collect images of the post-reaction surface.

Micro X-Ray Fluorescence Spectroscopy (µXRF). We used µXRF mapping to observe the distribution of mineral phases and elements in the rock chip both before and after carbonation, as well as to determine wt% oxide (**Table S2**) and elemental composition of sulfides (**Table S3**). µXRF analysis was performed on a Bruker Tornado M4 Plus instrument equipped with 2×60 mm^2 silicon drift detectors, and an automated XYZ positioner stage. A Rh x-ray source was used for data collection operating at 50kV and 600 uA, at a chamber pressure of 2 mbar. For chemical mapping, a pixel size of less than 20um was used along with an acquisition time of at least 25ms/pixel. All data were processed using the Bruker Espirit software and Bruker Advanced Mineral Analysis and Characterization System (AMICS) X-Ray microtomography (XMT) was then used to confirm the distribution of sulfides and silicates demonstrated in the AMICS results (**Figure S5**).

X-ray Photoelectron Spectroscopy (XPS). We performed XPS on the post-reaction surface of the chip to gain insight into the composition and valence of the top few nanometers of the rock. XPS is a surface-sensitive, non-destructive, quantitative spectroscopic technique capable of definitive carbonate identification that also provides insight into oxidation state of surface metals. XPS measurements were performed using a Thermo Fisher NEXSA spectrometer with a 125 mm mean radius, full 180° hemispherical analyzer, and 128-channel detector. This system uses a focused monochromatic Al Kα X-ray (1486.7 eV) source for excitation and an electron emission angle of 60 degrees. The narrow scan spectra were collected using a pass-energy of 50 eV with a step size of 0.1 eV. For the Ag $3d_{5/2}$ line, these conditions produced a FWHM of 0.84 eV ± 0.02 eV. The binding energy (BE) scale is calibrated using the Cu $2p_{3/2}$ feature at 932.62 ± 0.05 eV and Au $4f_{7/2}$ at 83.96 ± 0.05 eV.

Parr Vessel Experiments. The peridotite chip was reacted in a static batch experiment with wet $scCO_2$ in a 25 mL Parr vessel reactor. Water sufficient to saturate the $scCO_2$ was placed inside of the vessel and the chip was set on a Teflon tripod above and out of contact with the fluid. The vessel was then sealed and kept at temperature in a laboratory oven; trace oxygen was not removed from the reactor in order to simulate the redox conditions that would exist in field-based implementation. Once the vessel had equilibrated to 90 °C, it was pressurized with CO_2 to 9.0 MPa. These elevated conditions relative to typical geothermal-geobarometry gradients in the shallow crust were chosen to accelerate reaction kinetics for laboratory timescales. The chip was reacted under these conditions for 56 days, then recovered for mineralogical and compositional characterization.

Characterization and Feature Relocation Workflow Strategy. We characterized the Eagle Mine rock chip with several microscopy and spatially-resolved mineral identification methods to understand the starting mineralogy prior to carbonation. The chip was mapped first with µXRF, then SEM-EDS for

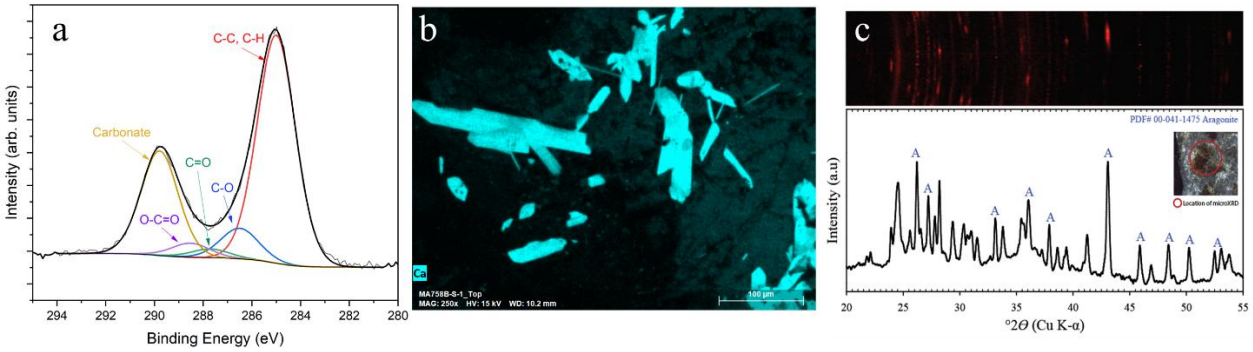

Figure 3. (a**)** XPS spectra of precipitated carbonate (b) EDS map (100 µm scale bar) of Ca-rich aragonite crystals (c) Region probed by µXRD to determine mineralogy of Ca-rich and Si-deficient crystals that appear as clustered translucent crystals in digital optical microscopy image (inset). Two-dimensional detector image showing diffraction rings and spots (top). Integration of the detector image to produce a diffractogram reveals the presence of peaks corresponding to aragonite ($CaCO_3$). The peak locations match with the International Centre for Diffraction Data powder diffraction file (PDF) entry for aragonite; PDF# 00-041-1475.

comparison and increased resolution of elemental maps. We then performed XPS on several points to gain information on speciation of sulfur, nickel, and carbonate phases on the surface. The chip was then reacted in a water-saturated, CO_2-dominant fluid in a Parr Vessel reactor for 56 days. The reacted chip was removed from the vessel and dried in an ambient temperature vacuum oven. XPS, the most surface-sensitive technique utilized, was conducted first to mitigate the potential of material deposited on the surface from other microscopy methods. The chip was then mapped with µXRF, then with SEM-EDS. Additional SEM images of neoformed precipitates and other areas of interest on the surface were also collected. Several areas of interest were then analyzed with µXRD. The workflow of pre- and post-reaction analyses developed for this study was the basis of our method development for similar comparison studies and is summarized in **Figure S1**. The relative sample activation volumes for the XPS, and EDS, and µXRF are shown schematically in **Figure S2**, emphasizing the complementary yet distinct nature of the analyses.

RESULTS AND DISCUSSION

Post-Reaction Feature Relocation. The mineralogy of the reacted sample consists of the original sulfide and silicate phases, which underwent partial dissolution, as well as precipitates deposited on the surface (**Figure S3)**. Comparison between µXRF element maps (Error! Reference source not found.) reveals changes in the distribution of several elements, specifically metals. Firstly, there are small areas of Ni in the post-reaction map not observed in the original element map. Several areas of Fe and Ca, confirmed with µXRD to be hematite (**Figure S4**) and aragonite (**Figure 3**) respectively, have also precipitated. Cations which formed these precipitates were predominantly released from the partial dissolution of olivine and plagioclase, based on the apparent partial dissolution of the silicates observed in post-reaction microscopy and µXRF maps for Ca and Si. Changes to the S distribution suggests that there was also partial dissolution of sulfide phases.

Carbon Mineralization. Initial XPS studies on the recovered Eagle Mine chip indicated that several areas of new precipitate consisted of carbonates (**Figure 3**), the majority of which µXRF mapping and SEM-EDS studies showed to be Ca-dominated. µXRD then confirmed that the Ca-carbonate phases was aragonite. The early formation of aragonite is consistent with previous diopside carbonation studies[20, 41], in which aragonite precipitation at 9.0 MPa $scCO_2$ conditions was observed via high-pressure time-resolved X-ray diffraction (50-110 °C) and identical location transmission electron microscopy (50 °C). Previous field and experimental studies of basalt carbonation paragenesis also indicated that aragonite is one of the first phases to form.[4, 5, 42] The preference for aragonite is expected based on the availability of magnesium in the system, which favors aragonite formation over calcite.[43] Overall, AMICS confirmed that the total amount of carbonate on the surface of the sample increased from 0.29 wt% to 0.83 wt%.

Fate of Nickel and Other Metals. Metals that were mobilized during carbonation and reprecipitated as mineral phases on the surface of the rock chip were characterized with XPS, µXRD, and SEM-EDS. Ni, the target critical metal of this study, was observed in precipitates along with Ca and Mn (**Figure 4**) that were not observed in the original mineralogy. These crystals are observed near original sulfides as well as potential dissolved and reprecipitated sulfides. The EDS spectra of these areas are suggestive of a potential carbonate phase but cannot be identified directly due to compositional contribution from the underlying substrate, though this composition would be consistent with divalent substitution in carbonate.

Iron was also readily mobilized in this reaction. Likely released from olivine, it partially precipitated as hematite and was found coating the remnants of original olivine grains (**Figure 2,** Fe and Si false color maps). This phase ID for hematite was also confirmed with µXRD (**Figure S4)**. Copper, potentially released in small amounts from original chalcopyrite or as trace amounts from silicate phases, was also observed and mapped using SEM-EDS (**Figure 4**). Cu, with lesser Fe, precipitated with S to form morphologies indicative of rapid growth (dendritic and wire-like precipitates are the most readily observed). Cu precipitation was also spatially related to the potential newly precipitated Ca-Mn-Ni carbonates.

Carbon Mineralization and Critical Mineral Recovery Potential of the Eagle Intrusion. The volume of the Eagle and East Eagle Intrusion is estimated to be 0.0666 km^3 (Eagle: ~480 m long, ~100-200 m wide, and >300 m vertical extension. East Eagle: ~600m long, ~150m wide, and >500m vertical extension).[44] Using this volume, a conservative estimate of Ni concentration in olivine (3000 ppm), and estimated volume of olivine in the rock (36.8%) (Table S1), , the total potential for carbon storage via mineralization and critical mineral recovery from olivine was calculated. The Eagle Intrusion can produce 27,000 metric tons (MT) of Ni, while storing 5 million metric tons (MMT) of CO_2. For context, the amount of Ni produced per year at the high grade mine at Eagle (~18,000 MT in 2022,)[45] indicating that CO_2 mineralization and enhanced mineral recovery (CO_2EMR) could compliment current high grade Ni

mining operations, or serve as an additional source of Ni after high grade ore has been exhausted and potentially extend life-of-mine

Low-Carbon Mineral Recovery. This work highlights the potential for a coupled carbon mineralization-critical mineral recovery process, but also reveals some of the key technological developments required to advance this technology to a pilot and subsequent commercial scale. The injection fluid in this experiment used only a H_2O-bearing CO_2 fluid, which resulted in elements of interest (i.e. Ni) being incorporated into carbonate phases. To extract the Ni for industrial use, the fluid will need to be engineered such that Ni remains in the fluid phase and is not mineralized, as demonstrated in our study. Current work on CO_2-EMR[36] suggests that the addition of Ni-complexing ligands can prevent its incorporation into phases such as carbonates.[27, 35] Additionally, only the surface of the chip reacted. Therefore, it may be necessary in low porosity ultramafic rocks to employ injection strategies that enhance the reactive surface area of the rock; engineered permeability and pore space optimization technologies from the mining, oil, and gas industries would likely compliment this approach.

ENVIRONMENTAL IMPLICATIONS

The integration of critical mineral recovery and carbon dioxide storage at current or former mine sites offers opportunities for climate smart mining. Climate smart mining involves sustainable extraction and processing of minerals to decrease the climate and material footprint of mining across the supply chain.[32, 46] The mining industry is currently responsible for 4-7% of global greenhouse gas emissions[47], and the approach presented here offers an opportunity for a carbon-intensive industry to decarbonize. Decarbonized mines, through in situ carbon storage and critical mineral recovery, offer an opportunity for climate smart mining in the extraction step of the mining supply chain while also reducing surface impacts and limiting water use.

The CO_2 for this climate-smart mining technology can either be sourced through point source capture or direct air capture (DAC) sources. This could either be sourced at the mine site or transported to the mine site via pipelines. Capturing and storing CO_2 underground at mines will offset carbon emissions associated with various stages of the supply chain including processing, refining, smelting, and transportation,

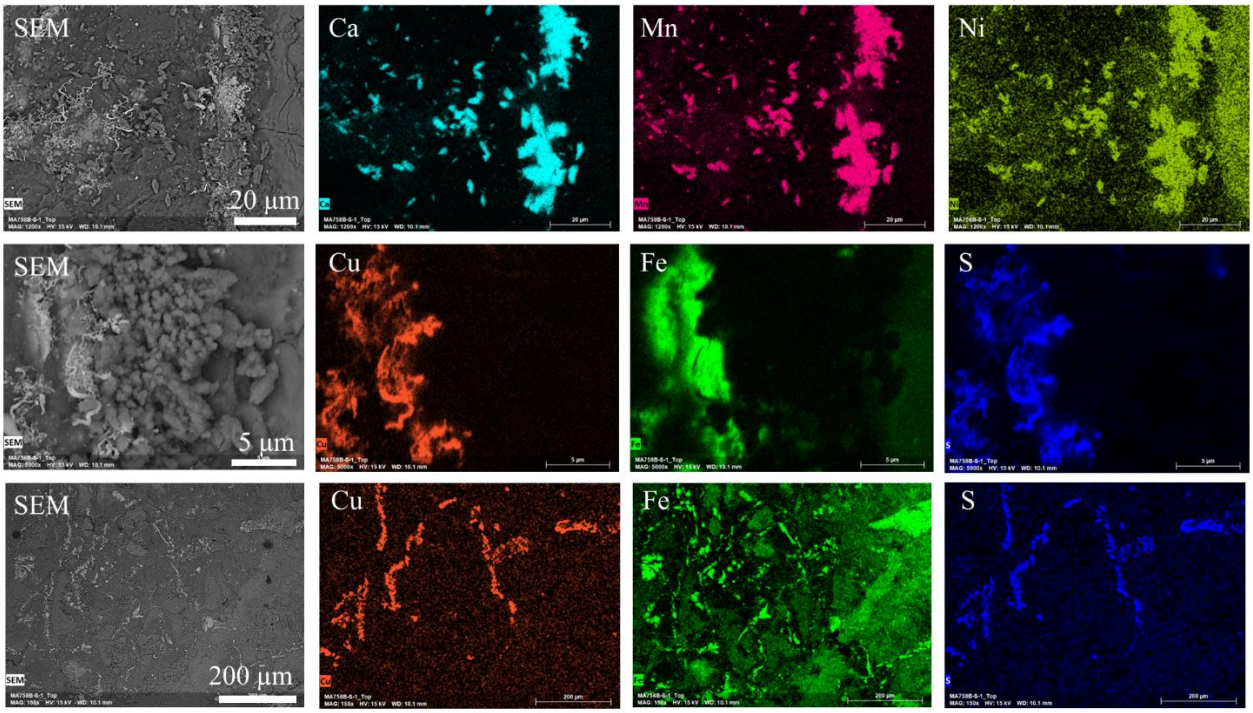

Figure 4. SEM images of three areas precipitated during carbonation, imaged with secondary electrons (greyscale) and then elementally mapped with EDS (false-color images). Scale bars present in greyscale images are consistent across rows. (d) Ca-Mn-Ni-bearing phase, likely carbonate. (e) Cu-Fe-S mineralization, interpreted as chalcopyrite based on elemental mapping. The morphology of this phase is indicative of quick growth, and this is interpreted as sulfide dissolution-reprecipitation. (f) Additional area of Cu-Fe sulfide that is not observed in the pre-reaction chip, which is indicative of sulfide reactivity.

potentially leading to carbon-neutral and carbon-negative mining.

ASSOCIATED CONTENT

Supplemental Information. This material is available free of charge on the ACS Publications website at http://pubs.acs.org. Characterization and experimental methodology workflow chart, schematic of XPS/EDS/XRF sample excitation volumes, pre- post-reaction optical images of reacted chip, microdiffraction data for reacted rock chip

AUTHOR INFORMATION

Corresponding Authors
*Corresponding Authors
M.A. Murchland madeline_murchland@mines.edu
Q.R.S. Miller quin.miller@pnnl.gov

Notes
The authors declare no competing financial interests.

ACKNOWLEDGEMENTS

This work was performed at the Pacific Northwest National Laboratory (PNNL), with DOE HQ support from Dr. Douglas Wicks and Dr. Emily Kinser and the Department of Energy (DOE) Advanced Research Projects-Energy (ARPA-e) MINER program under contract No. 22/CJ000/09/02. MAM was supported by the Mickey Leland Energy Fellowship through the DOE's Office of Fossil Energy and Carbon Management (FECM) and the Oak Ridge Institute for Science and Education (ORISE). We also thank Michael C. Perkins (PNNL) for his assistance with preparing the graphics. PNNL is operated by Battelle for the Department of Energy under contract no. DE-AC05-76RLO1830.

REFERENCES

(1) Metz, B.; Davidson, O.; De Coninck, H. C.; Loos, M.; Meyer, L. *IPCC special report on carbon dioxide capture and storage*; Cambridge: Cambridge University Press, 2005.
(2) Snæbjörnsdóttir, S. Ó.; Sigfússon, B.; Marieni, C.; Goldberg, D.; Gislason, S. R.; Oelkers, E. H. Carbon dioxide storage through mineral carbonation. *Nat. Rev. Earth Environ.* **2020**, *1* (2), 90-102. DOI: 10.1038/s43017-019-0011-8. McGrail, B. P.; Schaef, H. T.; Spane, F. A.; Cliff, J. B.; Qafoku, O.; Horner, J. A.; Thompson, C. J.; Owen, A. T.; Sullivan, C. E. Field Validation of Supercritical CO_2 Reactivity with Basalts. *Environmental Science & Technology Letters* **2017**, *4* (1), 6-10. DOI: 10.1021/acs.estlett.6b00387. Matter, J. M.; Stute, M.; Snaebjornsdottir, S. O.; Oelkers, E. H.; Gislason, S. R.; Aradottir, E. S.; Sigfusson, B.; Gunnarsson, I.; Sigurdardottir, H.; Gunnlaugsson, E.; et al. Rapid carbon mineralization for permanent disposal of anthropogenic carbon dioxide emissions. *Science* **2016**, *352* (6291), 1312-1314. DOI: 10.1126/science.aad8132. White, S. K.; Spane, F. A.; Schaef, H. T.; Miller, Q. R. S.; White, M. D.; Horner, J. A.; McGrail, B. P. Quantification of CO_2 Mineralization at the Wallula Basalt Pilot Project. *Environmental Science & Technology* **2020**, *54* (22), 14609-14616. DOI: 10.1021/acs.est.0c05142. Pogge von Strandmann, P. A. E.; Burton, K. W.; Snæbjörnsdóttir, S. O.; Sigfússon, B.; Aradóttir, E. S.; Gunnarsson, I.; Alfredsson, H. A.; Mesfin, K. G.; Oelkers, E. H.; Gislason, S. R. Rapid CO_2 mineralisation into calcite at the CarbFix storage site quantified using calcium isotopes. *Nature Communications* **2019**, *10* (1), 1983. DOI: 10.1038/s41467-019-10003-8. 44.01. *44.01 and ADNOC to scale up carbon mineralisation in the UAE*. 2024. https://www.4401.earth/blog/44-01-and-adnoc-to-scale-up-carbon-mineralisation-in-the-uae (accessed 2024 November 11). Oelkers, E. H.; Addassi, M.; Omar, A.; Afifi, A.; Hoteit, H.; Finkbeiner, T.; Menegoni, N.; Delaunay, A.; Fedorik, J.; Ahmed, Z. The successful carbon storage through subsurface mineral carbonation in the volcanic rocks near Jazan, Southwest Saudi Arabia. In *2024 Goldschmidt Conference*, 2024; GOLDSCHMIDT. Galeczka, I. M.; Stefánsson, A.; Kleine, B. I.; Gunnarsson-Robin, J.; Snæbjörnsdóttir, S. Ó.; Sigfússon, B.; Gunnarsdóttir, S. H.; Weisenberger, T. B.; Oelkers, E. H. A pre-injection assessment of CO2 and H2S mineralization reactions at the Nesjavellir (Iceland) geothermal storage site. *International Journal of Greenhouse Gas Control* **2022**, *115*, 103610. DOI: https://doi.org/10.1016/j.ijggc.2022.103610. Clark, D. E.; Oelkers, E. H.; Gunnarsson, I.; Sigfússon, B.; Snæbjörnsdóttir, S. Ó.; Aradottir, E. S.; Gíslason, S. R. CarbFix2: CO2 and H2S mineralization during 3.5 years of continuous injection into basaltic rocks at more than 250 C. *Geochimica et Cosmochimica Acta* **2020**, *279*, 45-66. Matter, J. M.; Takahashi, T.; Goldberg, D. Experimental evaluation of in situ CO_2-water-rock reactions during CO_2 injection in basaltic rocks: Implications for geological CO_2 sequestration. *Geochemistry Geophysics Geosystems* **2007**, *8*, Article. DOI: Q02001 10.1029/2006gc001427. Matter, J. M.; Takahashi, T.; Goldberg, D. Experimental evaluation of in situ CO2-water-rock reactions during CO2 injection in basaltic rocks: Implications for geological CO2 sequestration. *Geochemistry, Geophysics, Geosystems* **2007**, *8* (2). Xiong, W.; Wells, R. K.; Menefee, A. H.; Skemer, P.; Ellis, B. R.; Giammar, D. E. CO2 mineral trapping in fractured basalt. *International Journal of Greenhouse Gas Control* **2017**, *66*, 204-217. DOI: https://doi.org/10.1016/j.ijggc.2017.10.003. Wells, R. K.; Xiong, W.; Giammar, D.; Skemer, P. Dissolution and surface roughening of Columbia River flood basalt at geologic carbon sequestration conditions. *Chemical Geology* **2017**, *467*, 100-109. DOI: 10.1016/j.chemgeo.2017.07.028. Menefee, A. H.; Giammar, D. E.; Ellis, B. R. Permanent CO_2 Trapping through Localized and Chemical Gradient-Driven Basalt Carbonation. *Environmental Science & Technology* **2018**, *52* (15), 8954-8964. DOI: 10.1021/acs.est.8b01814. Wu, H.; Jayne, R. S.; Bodnar, R. J.; Pollyea, R. M. Simulation of CO2 mineral trapping and permeability alteration in fractured basalt: Implications for geologic carbon

sequestration in mafic reservoirs. *International Journal of Greenhouse Gas Control* **2021**, *109*, 103383. DOI: https://doi.org/10.1016/j.ijggc.2021.103383. Depp, C. T.; Miller, Q. R. S.; Crum, J. V.; Horner, J. A.; Schaef, H. T. Pore-scale Microenvironments Control Anthropogenic Carbon Mineralization Outcomes in Basalt. *ACS Earth and Space Chemistry* **2022**, *In Revision*. Lahiri, N.; Miller, Q. R. S.; Cao, R.; Depp, C. T.; Schaef, H. T. Facile Metal Release from Pore-Lining Phases Enables Unique Carbonate Zonation in a Basalt Carbon Mineralization Demonstration. *Environmental Science & Technology* **2023**, *57* (32), 11843-11851. DOI: 10.1021/acs.est.3c02075. Cao, R.; Miller, Q. R. S.; Davidson, C. L.; Gallin, W.; Reidel, S. P.; Jiao, Z.; McLaughlin, J. F.; Nienhuis, E. T.; Schaef, H. T. Gigaton commercial-scale carbon storage and mineralization potential in stacked Columbia River basalt reservoirs. *Int. J. Greenhouse Gas Control* **2024**, *137*, 104206. Cao, R.; Muller, K. A.; Miller, Q. R. S.; White, M. D.; Bacon, D. H.; Schaef, H. T. Reactive transport modeling of anthropogenic carbon mineralization in stacked Columbia River Basalt reservoirs. 2023, Unconventional Resources Technology Conference (URTeC): pp 1195-1202.

(3) Qomi, M. J. A.; Miller, Q. R. S.; Zare, S.; Schaef, H. T.; Kaszuba, J. P.; Rosso, K. M. Molecular-Scale Mechanisms of CO_2 Mineralization in Nanoscale Interfacial Water Films. *Nature Reviews Chemistry* **2022**, *6*, 598–613. DOI: https://doi.org/10.1038/s41570-022-00418-1.

(4) Xiong, W.; Wells, R. K.; Horner, J. A.; Schaef, H. T.; Skemer, P. A.; Giammar, D. E. CO_2 Mineral Sequestration in Naturally Porous Basalt. *Environmental Science & Technology Letters* **2018**, *5* (3), 142-147. DOI: 10.1021/acs.estlett.8b00047.

(5) Polites, E. G.; Schaef, H. T.; Horner, J. A.; Owen, A. T.; Holliman Jr, J. E.; McGrail, B. P.; Miller, Q. R. S. Exotic Carbonate Mineralization Recovered from a Deep Basalt Carbon Storage Demonstration. *Environmental Science & Technology* **2022**, *56* (20), 14713-14722.

(6) Li, X.; Nienhuis, E. T.; Nagurney, A. B.; Miller, Q. R.; Zhang, X.; Schaef, H. T. Resolving Nanoscale Processes during Carbon Mineralization Using Identical Location Transmission Electron Microscopy. *Environmental Science & Technology Letters* **2023**.

(7) García del Real, P.; Vishal, V. Mineral carbonation in ultramafic and basaltic rocks. *Geologic carbon sequestration: Understanding reservoir behavior* **2016**, 213-229. Matter, J. M.; Kelemen, P. B. Permanent storage of carbon dioxide in geological reservoirs by mineral carbonation. *Nature Geoscience* **2009**, *2* (12), 837-841.

(8) Goff, F.; Lackner, K. S. Carbon dioxide sequestering using ultramafic rocks. *Environmental Geosciences* **1998**, *5* (3), 89-101. Marini, L. *Geological sequestration of carbon dioxide: thermodynamics, kinetics, and reaction path modeling*; Elsevier, 2006.

(9) Stanfield, C. H.; Miller, Q. R. S.; Battu, A. K.; Lahiri, N.; Nagurney, A. B.; Cao, R.; Nienhuis, E. T.; DePaolo, D. J.; Latta, D. E.; Schaef, H. T. Carbon Mineralization and Critical Mineral Resource Evaluation Pathways for Mafic–Ultramafic Assets. *ACS Earth and Space Chemistry* **2024**, *8* (6), 1204-1213. DOI: 10.1021/acsearthspacechem.4c00005.

(10) Kelemen, P. B.; Matter, J.; Streit, E. E.; Rudge, J. F.; Curry, W. B.; Blusztajn, J. Rates and Mechanisms of Mineral Carbonation in Peridotite: Natural Processes and Recipes for Enhanced, in situ CO2 Capture and Storage. In *Annual Review of Earth and Planetary Sciences, Vol 39*, Jeanloz, R., Freeman, K. H. Eds.; Annual Review of Earth and Planetary Sciences, Vol. 39; 2011; pp 545-576. Peuble, S.; Andreani, M.; Gouze, P.; Pollet-Villard, M.; Reynard, B.; Van de Moortele, B. Multi-scale characterization of the incipient carbonation of peridotite. *Chemical Geology* **2017**. Kelemen, P. B.; Matter, J. In situ carbonation of peridotite for CO_2 storage. *Proceedings of the National Academy of Science* **2008**, *105* (45), 17295-17300. DOI: 10.1073/pnas.0805794105. Klein, F.; Garrido, C. J. Thermodynamic constraints on mineral carbonation of serpentinized peridotite. *Lithos* **2011**, *126* (3-4), 147-160. DOI: 10.1016/j.lithos.2011.07.020. Van Noort, R.; Spiers, C.; Drury, M.; Kandianis, M. Peridotite dissolution and carbonation rates at fracture surfaces under conditions relevant for in situ mineralization of CO2. *Geochimica et Cosmochimica Acta* **2013**, *106*, 1-24. Hövelmann, J.; Austrheim, H.; Beinlich, A.; Anne Munz, I. Experimental study of the carbonation of partially serpentinized and weathered peridotites. *Geochimica et Cosmochimica Acta* **2011**, *75* (22), 6760-6779. DOI: http://dx.doi.org/10.1016/j.gca.2011.08.032. Rudge, J. F.; Kelemen, P. B.; Spiegelman, M. A simple model of reaction-induced cracking applied to serpentinization and carbonation of peridotite. *Earth and Planetary Science Letters* **2010**, *291* (1-4), 215-227. Lacinska, A. M.; Styles, M. T.; Bateman, K.; Hall, M.; Brown, P. An experimental study of the carbonation of serpentinite and partially serpentinised peridotites. *Frontiers in Earth Science* **2017**, *5* (37), 37. DOI: 10.3389/feart.2017.00037. Grozeva, N. G.; Klein, F.; Seewald, J. S.; Sylva, S. P. Experimental study of carbonate formation in oceanic peridotite. *Geochimica et Cosmochimica Acta* **2017**, *199*, 264-286. DOI: http://dx.doi.org/10.1016/j.gca.2016.10.052. Menzel, M. D.; Garrido, C. J.; López Sánchez-Vizcaíno, V.; Marchesi, C.; Hidas, K.; Escayola, M. P.; Delgado Huertas, A. Carbonation of mantle peridotite by CO_2-rich fluids: the formation of listvenites in the Advocate ophiolite complex (Newfoundland, Canada). *Lithos* **2018**, *323*, 238-261. DOI: https://doi.org/10.1016/j.lithos.2018.06.001. Rahmani, O.; Highfield, J.; Junin, R.; Tyrer, M.; Pour, A. B. Experimental investigation and simplistic geochemical modeling of CO2 mineral carbonation using the mount tawai peridotite. *Molecules* **2016**, *21* (3), 353. Mervine, E. M.; Humphris, S. E.; Sims, K. W. W.; Kelemen, P. B.; Jenkins, W. J. Carbonation rates of peridotite in the Samail Ophiolite, Sultanate of Oman, constrained through 14C dating and stable isotopes. *Geochimica et Cosmochimica Acta* **2014**, *126*, 371-397. Paukert, A. N.; Matter, J. M.; Kelemen, P. B.; Shock, E. L.; Havig, J. R. Reaction path modeling of enhanced in situ CO2 mineralization for carbon sequestration in the peridotite of the Samail Ophiolite, Sultanate of Oman. *Chemical Geology* **2012**, *330*, 86-100. DOI: 10.1016/j.chemgeo.2012.08.013. Beinlich, A.; Austrheim, H. In situ sequestration of atmospheric CO2 at low temperature and surface cracking of serpentinized peridotite in mine shafts. *Chemical Geology* **2012**, *332*, 32-44, Article. DOI: 10.1016/j.chemgeo.2012.09.015. Decrausaz, T.; Godard, M.; Menzel, M. D.; Parat, F.; Oliot, E.; Lafay, R.; Barou, F.

Pervasive carbonation of peridotite to listvenite (Semail Ophiolite, Sultanate of Oman): clues from iron partitioning and chemical zoning. *European Journal of Mineralogy* **2023**, *35* (2), 171-187. Andreani, M.; Luquot, L.; Gouze, P.; Godard, M.; Hoise, E.; Gibert, B. Experimental Study of Carbon Sequestration Reactions Controlled by the Percolation of CO_2-Rich Brine through Peridotites. *Environmental Science & Technology* **2009**, *43* (4), 1226-1231. DOI: 10.1021/es8018429. Rigopoulos, I.; Harrison, A. L.; Delimitis, A.; Ioannou, I.; Efstathiou, A. M.; Kyratsi, T.; Oelkers, E. H. Carbon sequestration via enhanced weathering of peridotites and basalts in seawater. *Applied Geochemistry* **2018**, *91*, 197-207. DOI: 10.1016/j.apgeochem.2017.11.001. Tominaga, M.; Beinlich, A.; Lima, E. A.; Tivey, M. A.; Hampton, B. A.; Weiss, B.; Harigane, Y. Multi-scale magnetic mapping of serpentinite carbonation. *Nature communications* **2017**, *8* (1), 1870. Kelemen, P. B.; Aines, R.; Bennett, E.; Benson, S. M.; Carter, E.; Coggon, J. A.; De Obeso, J. C.; Evans, O.; Gadikota, G.; Dipple, G. M. In situ carbon mineralization in ultramafic rocks: Natural processes and possible engineered methods. *Energy Procedia* **2018**, *146*, 92-102. de Obeso, J. C.; Santiago Ramos, D. P.; Higgins, J. A.; Kelemen, P. B. A Mg isotopic perspective on the mobility of magnesium during serpentinization and carbonation of the Oman ophiolite. *Journal of Geophysical Research: Solid Earth* **2021**, *126* (2), e2020JB020237. Beinlich, A.; Plümper, O.; Boter, E.; Müller, I. A.; Kourim, F.; Ziegler, M.; Harigane, Y.; Lafay, R.; Kelemen, P. B.; Oman Drilling Project Science, T. Ultramafic rock carbonation: Constraints from listvenite core BT1B, Oman Drilling Project. *Journal of Geophysical Research: Solid Earth* **2020**, *125* (6), e2019JB019060. Okazaki, K.; Michibayashi, K.; Hatakeyama, K.; Abe, N.; Johnson, K. T.; Kelemen, P. B.; Team, O. D. P. S. Major Mineral Fraction and Physical Properties of Carbonated Peridotite (Listvenite) From ICDP Oman Drilling Project Hole BT1B Inferred From X-Ray CT Core Images. *Journal of Geophysical Research: Solid Earth* **2021**, *126* (12), e2021JB022719. Wilson, S.; Harrison, A. L.; Dipple, G. M.; Power, I. M.; Barker, S. L.; Mayer, K. U.; Fallon, S. J.; Raudsepp, M.; Southam, G. Offsetting of CO2 emissions by air capture in mine tailings at the Mount Keith Nickel Mine, Western Australia: Rates, controls and prospects for carbon neutral mining. *International Journal of Greenhouse Gas Control* **2014**, *25*, 121-140. Turvey, C. C.; Wilson, S. A.; Hamilton, J. L.; Southam, G. Field-based accounting of CO2 sequestration in ultramafic mine wastes using portable X-ray diffraction. *American Mineralogist* **2017**, *102* (6), 1302-1310. DOI: 10.2138/am-2017-5953. Oskierski, H. C.; Turvey, C. C.; Wilson, S.; Dlugogorski, B. Z.; Altarawneh, M.; Mavromatis, V. Mineralisation of atmospheric CO_2 in hydromagnesite in ultramafic mine tailings–Insights from Mg isotopes. *Geochim. Cosmochim. Acta* **2021**, *309*, 191-208.

(11) Hovelmann, J.; Austrheim, H.; Jamtveit, B. Microstructure and porosity evolution during experimental carbonation of a natural peridotite. *Chemical Geology* **2012**, *334*, 254-265, Article. DOI: 10.1016/j.chemgeo.2012.10.025. Klein, F.; McCollom, T. M. From serpentinization to carbonation: New insights from a CO_2 injection experiment. *Earth and Planetary Science Letters* **2013**, *379*, 137-145. DOI: 10.1016/j.epsl.2013.08.017.

(12) Power, I. M.; Paulo, C.; Rausis, K. The Mining Industry's Role in Enhanced Weathering and Mineralization for CO2 Removal. *Environmental Science & Technology* **2024**, *58* (1), 43-53. DOI: 10.1021/acs.est.3c05081.

(13) Miller, Q. R. S.; Schaef, H. T.; Kaszuba, J. P.; Qiu, L.; Bowden, M. E.; McGrail, B. P. Tunable Manipulation of Mineral Carbonation Kinetics in Nanoscale Water Films via Citrate Additives. *Environmental Science & Technology* **2018**, *52* (12), 7138-7148. DOI: 10.1021/acs.est.8b00438.

(14) Miller, Q. R. S.; Kaszuba, J. P.; Schaef, H. T.; Bowden, M. E.; McGrail, B. P. Impacts of organic ligands on forsterite reactivity in supercritical CO_2 fluids. *Environmental Science & Technology* **2015**, *49* (7), 4724-4734. DOI: 10.1021/es506065d.

(15) Rimstidt, J. D.; Brantley, S. L.; Olsen, A. A. Systematic review of forsterite dissolution rate data. *Geochimica et Cosmochimica Acta* **2012**, *99*, 159-178. DOI: 10.1016/j.gca.2012.09.019. Crundwell, F. K. The mechanism of dissolution of forsterite, olivine and minerals of the orthosilicate group. *Hydrometallurgy* **2014**, *150*, 68-82, Article. DOI: 10.1016/j.hydromet.2014.09.006 Scopus. Oelkers, E. H.; Declercq, J.; Saldi, G. D.; Gislason, S. R.; Schott, J. Olivine dissolution rates: A critical review. *Chem. Geol.* **2018**, *500*, 1-19. Palandri, J. L.; Kharaka, Y. K. *A compilation of rate parameters of water-mineral interaction kinetics for application to geochemical modeling*; 2004-1068; United States Geological Survey, Menlo Park, California, 2004.

(16) Gerdemann, S. J.; O'Connor, W. K.; Dahlin, D. C.; Penner, L. R.; Rush, H. Ex Situ Aqueous Mineral Carbonation. *Environmental Science & Technology* **2007**, *41* (7), 2587-2593. DOI: 10.1021/es0619253. Lafay, R.; Montes-Hernandez, G.; Janots, E.; Chiriac, R.; Findling, N.; Toche, F. Simultaneous precipitation of magnesite and lizardite from hydrothermal alteration of olivine under high-carbonate alkalinity. *Chemical Geology* **2014**, *368*, 63-75. DOI: 10.1016/j.chemgeo.2014.01.008. Jones, L. C.; Rosenbauer, R.; Goldsmith, J. I.; Oze, C. Carbonate control of H_2 and CH_4 production in serpentinization systems at elevated P-Ts. *Geophysical Research Letters* **2010**, *37*, L14306. DOI: 10.1029/2010gl043769. Přikryl, J.; Stefánsson, A.; Pearce, C. R. Tracing olivine carbonation and serpentinization in CO_2-rich fluids via magnesium exchange and isotopic fractionation. *Geochimica et Cosmochimica Acta* **2018**, *243*, 133-148. DOI: https://doi.org/10.1016/j.gca.2018.09.022. Gadikota, G.; Matter, J.; Kelemen, P.; Park, A.-h. A. Chemical and morphological changes during olivine carbonation for CO_2 storage in the presence of NaCl and $NaHCO_3$. *Physical Chemistry Chemical Physics* **2014**, *16* (10), 4679-4693, 10.1039/C3CP54903H. DOI: 10.1039/C3CP54903H. Eikeland, E.; Blichfeld, A. B.; Tyrsted, C.; Jensen, A.; Iversen, B. B. Optimized carbonation of magnesium silicate mineral for CO_2 storage. *ACS Applied Materials & Interfaces* **2015**, *7* (9), 5258-5264. Ueda, H.; Sawaki, Y.; Maruyama, S. Reactions between olivine and CO_2-rich seawater at 300 °C: Implications for H_2 generation and CO_2 sequestration on the early Earth. *Geoscience Frontiers*

2017, *8* (2), 387-396. DOI: 10.1016/j.gsf.2016.10.002. McCollom, T. M.; Klein, F.; Robbins, M.; Moskowitz, B.; Berquo, T. S.; Jons, N.; Bach, W.; Templeton, A. Temperature trends for reaction rates, hydrogen generation, and partitioning of iron during experimental serpentinization of olivine. *Geochim. Cosmochim. Acta* **2016**, *181*, 175-200. DOI: 10.1016/j.gca.2016.03.002. Turri, L.; Muhr, H.; Rijnsburger, K.; Knops, P.; Lapicque, F. CO_2 sequestration by high pressure reaction with olivine in a rocking batch autoclave. *Chem. Eng. Sci.* **2017**, *171*, 27-31. DOI: https://doi.org/10.1016/j.ces.2017.05.009. Sekine, Y.; Shibuya, T.; Postberg, F.; Hsu, H. W.; Suzuki, K.; Masaki, Y.; Kuwatani, T.; Mori, M.; Hong, P. K.; Yoshizaki, M.; et al. High-temperature water-rock interactions and hydrothermal environments in the chondrite-like core of Enceladus. *Nature Communications* **2015**, *6*, 8604. DOI: 10.1038/ncomms9604. Sissmann, O.; Brunet, F.; Martinez, I.; Guyot, F.; Verlaguet, A.; Pinquier, Y.; Daval, D. Enhanced Olivine Carbonation within a Basalt as Compared to Single-Phase Experiments: Reevaluating the Potential of CO_2 Mineral Sequestration. *Environmental Science & Technology* **2014**, *48* (10), 5512-5519. DOI: 10.1021/es405508a (acccessed 2014/05/14). Miller, Q. R. S.; Schaef, H. T. Activation energy of magnesite ($MgCO_3$) precipitation: recent insights from olivine carbonation studies. *Environmental Science: Advances* **2022**, *1*, 426-429. DOI: https://doi.org/10.1039/D2VA00066K. Sendula, E.; Lamadrid, H. M.; Rimstidt, J. D.; Steele-MacInnis, M.; Sublett, D. M.; Aradi, L. E.; Szabó, C.; Caddick, M. J.; Zajacz, Z.; Bodnar, R. J. Synthetic Fluid Inclusions XXIV. In situ Monitoring of the Carbonation of Olivine Under Conditions Relevant to Carbon Capture and Storage Using Synthetic Fluid Inclusion Micro-Reactors: Determination of Reaction Rates. *Frontiers in Climate* **2021**, *3* (134), 722447, Original Research. DOI: 10.3389/fclim.2021.722447. Xing, T.; Zhu, W.; Fusseis, F.; Lisabeth, H. Generating porosity during olivine carbonation via dissolution channels and expansion cracks. *Solid Earth* **2018**, *9* (4), 879–896. Wells, R. K.; Xiong, W.; Sesti, E.; Cui, J.; Giammar, D.; Skemer, P.; Hayes, S. E.; Conradi, M. S. Spatially-variable carbonation reactions in polycrystalline olivine. *Geochimica et Cosmochimica Acta* **2017**, *204*, 252-266. DOI: http://dx.doi.org/10.1016/j.gca.2017.02.003. Cui, J. L.; Sesti, E. L.; Moore, J. K.; Giammar, D. E.; Hayes, S. E. Evidence from ^{29}Si Solid-State Nuclear Magnetic Resonance of Dissolution Reactions of Forsterite. *Environmental Engineering Science* **2016**, *33* (10), 799-805, Article. DOI: 10.1089/ees.2016.0004. Saldi, G. D.; Daval, D.; Guo, H.; Guyot, F.; Bernard, S.; Le Guillou, C.; Davis, J. A.; Knauss, K. G. Mineralogical evolution of Fe-Si-rich layers at the olivine-water interface during carbonation reactions. *American Mineralogist* **2015**, *100* (11-12), 2655-2669. DOI: 10.2138/am-2015-5340. Johnson, N. C.; Thomas, B.; Maher, K.; Rosenbauer, R. J.; Bird, D.; Brown, G. E., Jr. Olivine dissolution and carbonation under conditions relevant for in situ carbon storage. *Chemical Geology* **2014**, *373*, 93-105. DOI: 10.1016/j.chemgeo.2014.02.026. Olsson, J.; Bovet, N.; Makovicky, E.; Bechgaard, K.; Balogh, Z.; Stipp, S. L. S. Olivine reactivity with CO2 and H2O on a microscale: Implications for carbon sequestration. *Geochimica Et Cosmochimica Acta* **2012**, *77*, 86-97, Article. DOI: 10.1016/j.gca.2011.11.001. King, H. E.; Plumper, O.; Putnis, A. Effect of Secondary Phase Formation on the Carbonation of Olivine. *Environmental Science & Technology* **2010**, *44* (16), 6503-6509. DOI: 10.1021/es9038193. Prigiobbe, V.; Hänchen, M.; Werner, M.; Baciocchi, R.; Mazzotti, M. Mineral carbonation process for CO2 sequestration. *Energy Procedia* **2009**, *1* (1), 4885. Bearat, H.; McKelvy, M.; Chizmeshya, A.; Gormley, D.; Nunez, R.; Carpenter, R.; Squires, K.; Wolf, G. Carbon Sequestration via Aqueous Olivine Mineral Carbonation: Role of Passivating Layer Formation. *Environ Sci Technol* **2006**, *40*, 4802-4802. Xiong, W.; Wells, R. K.; Giammar, D. E. Carbon Sequestration in Olivine and Basalt Powder Packed Beds. *Environmental Science & Technology* **2017**, *51* (4), 2105-2112. DOI: 10.1021/acs.est.6b05011. Adeoye, J. T.; Menefee, A. H.; Xiong, W.; Wells, R. K.; Skemer, P.; Giammar, D. E.; Ellis, B. R. Effect of transport limitations and fluid properties on reaction products in fractures of unaltered and serpentinized basalt exposed to high PCO2 fluids. *International Journal of Greenhouse Gas Control* **2017**, *63*, 310-320. DOI: https://doi.org/10.1016/j.ijggc.2017.06.003. Menefee, A. H.; Ellis, B. R. Carbon Mineralization in Reactive Silicate Zones. *ACS ES&T Engineering* **2021**, *1* (8), 1193-1204. DOI: 10.1021/acsestengg.1c00066. Giammar, D. E.; Bruant, R. G.; Peters, C. A. Forsterite dissolution and magnesite precipitation at conditions relevant for deep saline aquifer storage and sequestration of carbon dioxide. *Chemical Geology* **2005**, *217* (3-4), 257-276. DOI: 10.1016/j.chemgeo.2004.12.013.

(17) Miller, Q. R. S.; Kaszuba, J. P.; Schaef, H. T.; Bowden, M. E.; McGrail, B. P.; Rosso, K. M. Anomalously low activation energy of nanoconfined $MgCO_3$ precipitation. *Chemical Communications* **2019**, *55* (48), 6835-6837, 10.1039/C9CC01337G. DOI: 10.1039/C9CC01337G.

(18) Gadikota, G.; Matter, J.; Kelemen, P.; Brady, P. V.; Park, A.-H. A. Elucidating the differences in the carbon mineralization behaviors of calcium and magnesium bearing alumino-silicates and magnesium silicates for CO2 storage. *Fuel* **2020**, *277*, 117900. DOI: https://doi.org/10.1016/j.fuel.2020.117900. Wang, F.; Dreisinger, D.; Jarvis, M.; Hitchins, T. Kinetic evaluation of mineral carbonation of natural silicate samples. *Chemical Engineering Journal* **2021**, *404*, 126522. DOI: https://doi.org/10.1016/j.cej.2020.126522.

(19) Placencia-Gómez, E.; Kerisit, S. N.; Mehta, H. S.; Qafoku, O.; Thompson, C. J.; Graham, T. R.; Ilton, E. S.; Loring, J. S. Critical Water Coverage during Forsterite Carbonation in Thin Water Films: Activating Dissolution and Mass Transport. *Environmental Science & Technology* **2020**, *54* (11), 6888-6899. DOI: 10.1021/acs.est.0c00897. Kerisit, S. N.; Mergelsberg, S. T.; Thompson, C. J.; White, S. K.; Loring, J. S. Thin Water Films Enable Low-Temperature Magnesite Growth Under Conditions Relevant to Geologic Carbon Sequestration. *Environmental Science & Technology* **2021**, *55* (18), 12539-12548. DOI: 10.1021/acs.est.1c03370. Mergelsberg, S. T.; Kerisit, S. N.; Ilton, E. S.; Qafoku, O.; Thompson, C. J.; Loring, J. S. Low temperature and limited water activity reveal a pathway to

magnesite via amorphous magnesium carbonate. *Chemical Communications* **2020**, *56* (81), 12154-12157, 10.1039/D0CC04907G. DOI: 10.1039/D0CC04907G. Mergelsberg, S. T.; Rajan, B. P.; Legg, B. A.; Kovarik, L.; Burton, S. D.; Bowers, G. M.; Bowden, M. E.; Qafoku, O.; Thompson, C. J.; Kerisit, S. N.; et al. Nanoscale Mg-Depleted Layers Slow Carbonation of Forsterite (Mg2SiO4) When Water Is Limited. *Environmental Science & Technology Letters* **2023**, *10* (1), 98-104. DOI: 10.1021/acs.estlett.2c00866. Loring, J. S.; Chen, J.; Benezeth, P.; Qafoku, O.; Ilton, E. S.; Washton, N. M.; Thompson, C. J.; Martin, P. F.; McGrail, B. P.; Rosso, K. M.; et al. Evidence for carbonate surface complexation during forsterite carbonation in wet supercritical carbon dioxide. *Langmuir* **2015**, *31* (27), 7533-7543. DOI: 10.1021/acs.langmuir.5b01052. Thompson, C. J.; Martin, P. F.; Chen, J.; Benezeth, P.; Schaef, H. T.; Rosso, K. M.; Felmy, A. R.; Loring, J. S. Automated high-pressure titration system with in situ infrared spectroscopic detection. *Review of Scientific Instruments* **2014**, *85* (4), 044102. DOI: 10.1063/1.4870411. Miller, Q. R. S.; Kaszuba, J. P.; Kerisit, S. N.; Schaef, H. T.; Bowden, M. E.; McGrail, B. P.; Rosso, K. M. Emerging investigator series: ion diffusivities in nanoconfined interfacial water films contribute to mineral carbonation thresholds. *Environmental Science: Nano* **2020**, *7* (4), 1068-1081, 10.1039/C9EN01382B. DOI: 10.1039/C9EN01382B. Felmy, A. R.; Qafoku, O.; Arey, B. W.; Hu, J. Z.; Hu, M.; Todd Schaef, H.; Ilton, E. S.; Hess, N. J.; Pearce, C. I.; Feng, J.; et al. Reaction of water-saturated supercritical CO_2 with forsterite: Evidence for magnesite formation at low temperatures. *Geochimica et Cosmochimica Acta* **2012**, *91*, 271-282. DOI: 10.1016/j.gca.2012.05.026. Wang, Z.; Felmy, A. R.; Thompson, C. J.; Loring, J. S.; Joly, A. G.; Rosso, K. M.; Schaef, H. T.; Dixon, D. A. Near-infrared spectroscopic investigation of water in supercritical CO_2 and the effect of $CaCl_2$. *Fluid Phase Equilibria* **2013**, *338*, 155-163. DOI: 10.1016/j.fluid.2012.11.012. Loring, J. S.; Thompson, C. J.; Wang, Z.; Joly, A. G.; Sklarew, D. S.; Schaef, H. T.; Ilton, E. S.; Rosso, K. M.; Felmy, A. R. In Situ Infrared Spectroscopic Study of Forsterite Carbonation in Wet Supercritical CO2. *Environmental Science & Technology* **2011**, *45* (14), 6204-6210. DOI: 10.1021/es201284e. Qafoku, O.; Hu, J.; Hess, N. J.; Hu, M. Y.; Ilton, E. S.; Feng, J.; Arey, B. W.; Felmy, A. R. Formation of submicron magnesite during reaction of natural forsterite in H_2O-saturated supercritical CO_2. *Geochimica et Cosmochimica Acta* **2014**, *134*, 197-209. DOI: 10.1016/j.gca.2013.09.024. Schaef, H. T.; McGrail, B. P.; Loring, J. L.; Bowden, M. E.; Arey, B. W.; Rosso, K. M. Forsterite [Mg_2SiO_4)] Carbonation in Wet Supercritical CO_2: An in Situ High-Pressure X-ray Diffraction Study. *Environmental Science & Technology* **2013**, *47* (1), 174-181. DOI: 10.1021/es301126f. Miller, Q. R. S.; Dixon, D. A.; Burton, S. D.; Walter, E. D.; Hoyt, D. W.; McNeill, A. S.; Moon, J. D.; Thanthiriwatte, K. S.; Ilton, E. S.; Qafoku, O.; et al. Surface-Catalyzed Oxygen Exchange during Mineral Carbonation in Nanoscale Water Films. *The Journal of Physical Chemistry C* **2019**, *123* (20), 12871-12885. DOI: 10.1021/acs.jpcc.9b02215. Qafoku, O.; Kovarik, L.; Kukkadapu, R. K.; Ilton, E. S.; Arey, B. W.; Tucek, J.; Felmy, A. R. Fayalite dissolution and siderite formation in water-saturated supercritical CO_2. *Chemical Geology* **2012**, *332*, 124-135, Article. DOI: 10.1016/j.chemgeo.2012.09.028.

(20) Li, X.; Nienhuis, E. T.; Nagurney, A. B.; Miller, Q. R. S.; Zhang, X.; Schaef, H. T. Resolving Nanoscale Processes during Carbon Mineralization Using Identical Location Transmission Electron Microscopy. *Environmental Science & Technology Letters* **2023**. DOI: 10.1021/acs.estlett.3c00699.

(21) Bouissonnié, A.; Daval, D.; Ackerer, P. Dissolution Anisotropy of Pyroxenes: A Surrogate Model for Steady-State Enstatite Dissolution Resulting from Stochastic Simulations of the Hydrolysis Process. *The Journal of Physical Chemistry C* **2020**, *124* (24), 13113-13126. DOI: 10.1021/acs.jpcc.0c00962. Bouissonnié, A.; Daval, D.; Ackerer, P. Dissolution Anisotropy of Pyroxenes: Role of Edges and Corners Inferred from Stochastic Simulations of Enstatite Dissolution. *The Journal of Physical Chemistry C* **2021**, *125* (14), 7658-7674. DOI: 10.1021/acs.jpcc.0c11416. Bouissonnié, A.; Daval, D.; Guyot, F.; Ackerer, P. The Dissolution Anisotropy of Pyroxenes: Experimental Validation of a Stochastic Dissolution Model Based on Enstatite Dissolution. *The Journal of Physical Chemistry C* **2020**, *124* (5), 3122-3140. DOI: 10.1021/acs.jpcc.9b10824. Daval, D.; Hellmann, R.; Saldi, G. D.; Wirth, R.; Knauss, K. G. Linking nm-scale measurements of the anisotropy of silicate surface reactivity to macroscopic dissolution rate laws: New insights based on diopside. *Geochimica et Cosmochimica Acta* **2013**, *107*, 121-134. Phillips-Lander, C. M.; Elwood Madden, A. S.; Hausrath, E. M.; Elwood Madden, M. E. Aqueous alteration of pyroxene in sulfate, chloride, and perchlorate brines: Implications for post-Noachian aqueous alteration on Mars. *Geochimica et Cosmochimica Acta* **2019**, *257*, 336-353. DOI: https://doi.org/10.1016/j.gca.2019.05.006. Knauss, K. G.; Nguyen, S. N.; Weed, H. C. Diopside dissolution kinetics as a function of pH, CO_2, temperature, and time. *Geochim. Cosmochim. Acta* **1993**, *57* (2), 285-294. Siegel, D. I.; Pfannkuch, H. O. Silicate mineral dissolution at pH 4 and near standard temperature and pressure. *Geochimica et Cosmochimica Acta* **1984**, *48* (1), 197-201. Schott, J.; Berner, R. A. Dissolution mechanisms of pyroxenes and olivines during weathering. In *The chemistry of weathering*, Springer, 1985; pp 35-53. Petit, J.-C.; Mea, G. D.; Dran, J.-C.; Schott, J.; Berner, R. A. Mechanism of diopside dissolution from hydrogen depth profiling. *Nature* **1987**, *325* (6106), 705-707. Schott, J.; Berner, R. A.; Sjöberg, E. L. Mechanism of pyroxene and amphibole weathering—I. Experimental studies of iron-free minerals. *Geochim. Cosmochim. Acta* **1981**, *45* (11), 2123-2135. DOI: https://doi.org/10.1016/0016-7037(81)90065-X. Oelkers, E. H. A Comparison of Forsterite and Enstatite Dissolution Rates and Mechanisms. In *Growth, Dissolution and Pattern Formation in Geosystems*, Jamtveit, B., Meakin, P. Eds.; Springer Netherlands, 1999; pp 253-267 . Oelkers, E. H.; Schott, J. An experimental study of enstatite dissolution rates as a function of pH, temperature, and aqueous Mg and Si concentration, and the mechanism of pyroxene/pyroxenoid dissolution. *Geochimica et Cosmochimica Acta* **2001**, *65* (8), 1219-1231, Journal. Sverdrup, H. U. *The kinetics of base cation release due to*

chemical weathering; Krieger Publishing Company, 1990. Dixit, S.; Carroll, S. A. Effect of solution saturation state and temperature on diopside dissolution. *Geochem. Trans.* **2007**, *8* (1), 1-14. Chen, Y.; Brantley, S. L. Diopside and anthophyllite dissolution at 25° and 90°C and acid pH. *Chemical Geology* **1998**, *147*, 233-248, Journal. Brantley, S. L.; Chen, Y. Chemical weathering rates of pyroxenes and amphiboles. In *Chemical weathering rates of silicate minerals*, White, A. F., Brantley, S. L. Eds.; Reviews in Mineralogy, Vol. 31; Mineralogical Society of America, 1995; pp 119-172. Monasterio-Guillot, L.; Rodriguez-Navarro, C.; Ruiz-Agudo, E. Kinetics and Mechanisms of Acid-pH Weathering of Pyroxenes. *Geochemistry, Geophysics, Geosystems* **2021**, *22* (11), e2021GC009711, https://doi.org/10.1029/2021GC009711. DOI: https://doi.org/10.1029/2021GC009711 (acccessed 2022/01/08). Heřmanská, M.; Voigt, M. J.; Marieni, C.; Declercq, J.; Oelkers, E. H. A comprehensive and internally consistent mineral dissolution rate database: Part I: Primary silicate minerals and glasses. *Chem. Geol.* **2022**, *597*, 120807. DOI: https://doi.org/10.1016/j.chemgeo.2022.120807. Stockmann, G.; Wolff-Boenisch, D.; Gislason, S. R.; Oelkers, E. H. Dissolution of diopside and basaltic glass: the effect of carbonate coating. *Mineralogical Magazine* **2008**, *72* (1), 135-139. DOI: 10.1180/minmag.2008.072.1.135. Daval, D.; Hellmann, R.; Corvisier, J.; Tisserand, D.; Martinez, I.; Guyot, F. Dissolution kinetics of diopside as a function of solution saturation state: Macroscopic measurements and implications for modeling of geological storage of CO_2. *Geochimica et Cosmochimica Acta* **2010**, *74* (9), 2615-2633. DOI: https://doi.org/10.1016/j.gca.2010.02.003. Stockmann, G. J.; Wolff-Boenisch, D.; Gislason, S. R.; Oelkers, E. H. Do carbonate precipitates affect dissolution kinetics?: 2: Diopside. *Chemical Geology* **2013**, *337-338*, 56-66. DOI: https://doi.org/10.1016/j.chemgeo.2012.11.014.

(22) Bodor, M.; Santos, R. M.; Kriskova, L.; Elsen, J.; Vlad, M.; Van Gerven, T. Susceptibility of mineral phases of steel slags towards carbonation: mineralogical, morphological and chemical assessment. *European Journal of Mineralogy* **2013**, *25* (4), 533-549, Article; Proceedings Paper. DOI: 10.1127/0935-1221/2013/0025-2300. Chai, Y. E.; Miller, Q. R. S.; Schaef, H. T.; Barpaga, D.; Bakhshoodeh, R.; Bodor, M.; Van Gerven, T.; Santos, R. M. Pressurized in situ X-ray diffraction insights into super/subcritical carbonation reaction pathways of steelmaking slags and constituent silicate minerals. *J. Supercrit. Fluids* **2021**, *171*, 105191. DOI: https://doi.org/10.1016/j.supflu.2021.105191. Loring, J. S.; Miller, Q. R. S.; Schaef, H. T.; Thompson, C. J. Experimental studies of reactivity and transformations of rocks and minerals in water-bearing supercritical CO_2. In *Science of Carbon Storage in Deep Saline Formations: Process Coupling across Time and Spatial Scales*, 1st ed.; Newell, P., Ilgen, A. G. Eds.; Elsevier, 2018. Monasterio-Guillot, L.; Di Lorenzo, F.; Ruiz-Agudo, E.; Rodriguez-Navarro, C. Reaction of pseudowollastonite with carbonate-bearing fluids: Implications for CO_2 mineral sequestration. *Chemical Geology* **2019**, *524*, 158-173. DOI: https://doi.org/10.1016/j.chemgeo.2019.06.011. Monasterio-Guillot, L.; Fernandez-Martinez, A.; Ruiz-Agudo, E.; Rodriguez-Navarro, C. Carbonation of calcium-magnesium pyroxenes: Physical-chemical controls and effects of reaction-driven fracturing. *Geochimica et Cosmochimica Acta* **2021**, *304*, 258-280. DOI: https://doi.org/10.1016/j.gca.2021.02.016. Schaef, H. T.; Miller, Q. R. S.; Thompson, C. J.; Loring, J. S.; Bowden, M. S.; Arey, B. W.; McGrail, B. P.; Rosso, K. M. Silicate carbonation in supercritical CO_2 containing dissolved H_2O: An in situ high pressure X-ray diffraction and infrared spectroscopy study. *Energy Procedia* **2013**, *37* (0), 5892-5896. DOI: http://dx.doi.org/10.1016/j.egypro.2013.06.514. Jiang, D.; Dong, S.; Zhao, L.; Teng, H. The Mechanism of Diopside-Water-Supercritical CO_2 Reaction: Relevance to CO_2 Sequestration. In *American Geophysical Union Fall Meeting*, San Francisco, CA, 2013, 2013; Vol. 2013, pp MR33B-2336. Kalinkin, A. M.; Politov, A. A.; Boldyrev, V. V.; Kalinkina, E. V.; Makarov, V. N.; Kalinnikov, V. T. Mechanical Activation of Diopside in CO2. *Inorganic Materials* **2002**, *38* (2), 163-167. DOI: 10.1023/A:1014021312359.

(23) Aguila, B.; Hardee, L.; Schaef, H. T.; Zare, S.; Abdolhosseini Qomi, M. J.; Crum, J. V.; Holliman Jr, J. E.; Rodriguez, E. T.; Anovitz, L. M.; Rosso, K. M.; et al. Emerging investigator series: kinetics of diopside reactivity for carbon mineralization in mafic–ultramafic rocks. *Environ. Sci. Nano* **2023**, *10* (10), 2672-2684, 10.1039/D3EN00087G. DOI: 10.1039/D3EN00087G.

(24) de Obeso, J. C.; Awolayo, A. N.; Nightingale, M. J.; Tan, C.; Tutolo, B. M. Experimental study on plagioclase dissolution rates at conditions relevant to mineral carbonation of seafloor basalts. *Chemical Geology* **2023**, *620*, 121348. Min, Y.; Kubicki, J. D.; Jun, Y.-S. Plagioclase dissolution during CO2–SO2 cosequestration: Effects of sulfate. *Environmental Science & Technology* **2015**, *49* (3), 1946-1954. Gudbrandsson, S.; Wolff-Boenisch, D.; Gislason, S. R.; Oelkers, E. H. Experimental determination of plagioclase dissolution rates as a function of its composition and pH at 22°C. *Geochimica et Cosmochimica Acta* **2014**, *139*, 154-172. DOI: https://doi.org/10.1016/j.gca.2014.04.028. Zhang, L.; Luettge, A. Theoretical approach to evaluating plagioclase dissolution mechanisms. *Geochimica Et Cosmochimica Acta* **2009**, *73* (10), 2832-2849. DOI: 10.1016/j.gca.2009.02.021. Oxburgh, R.; Drever, J. I.; Sun, Y.-T. Mechanism of plagioclase dissolution in acid solution at 25°C. *Geochimica et Cosmochimica Acta* **1994**, *58* (2), 661-669. DOI: https://doi.org/10.1016/0016-7037(94)90496-0. Welch, S. A.; Ullman, W. J. The effect of organic acids on plagioclase dissolution rates and stoichiometry. *Geochimica et Cosmochimica Acta* **1993**, *57* (12), 2725-2736. DOI: https://doi.org/10.1016/0016-7037(93)90386-B. Casey, W. H.; Westrich, H. R.; Holdren, G. R. Dissolution rates of plagioclase at pH= 2 and 3. *American Mineralogist* **1991**, *76* (1-2), 211-217. Jordan, G.; Higgins, S. R.; Eggleston, C. M.; Swapp, S. M.; Janney, D. E.; Knauss, K. G. Acidic dissolution of plagioclase: In-situ observations by hydrothermal atomic force microscopy. *Geochimica et Cosmochimica Acta* **1999**, *63* (19-20), 3183-3191. DOI: 10.1016/s0016-7037(99)00225-2. Huang, W. H.; Kiang, W. C. Laboratory dissolution of plagioclase feldspars in water and organic acids at room

temperature. *American Mineralogist: Journal of Earth and Planetary Materials* **1972**, *57* (11-12), 1849-1859. Seyama, H.; Kinoshita, K.; Soma, M. Surface alteration of plagioclase during acid dissolution. *Surface and Interface Analysis* **2002**, *34* (1), 289-292. DOI: https://doi.org/10.1002/sia.1302 (acccessed 2024/01/20). Yang, Y.; Min, Y.; Jun, Y.-S. A mechanistic understanding of plagioclase dissolution based on Al occupancy and T–O bond length: from geologic carbon sequestration to ambient conditions. *Physical Chemistry Chemical Physics* **2013**, *15* (42), 18491-18501. Oelkers, E. H.; Schott, J. Experimental study of anorthite dissolution and the relative mechanism of feldspar hydrolysis. *Geochimica et Cosmochimica Acta* **1995**, *59* (24), 5039-5053.

(25) Munz, I. A.; Brandvoll, Ø.; Haug, T.; Iden, K.; Smeets, R.; Kihle, J.; Johansen, H. Mechanisms and rates of plagioclase carbonation reactions. *Geochimica et Cosmochimica Acta* **2012**, *77*, 27-51. Hangx, S. J. T.; Spiers, C. J. Reaction of plagioclase feldspars with CO2 under hydrothermal conditions. *Chemical Geology* **2009**, *265* (1-2), 88-98. DOI: 10.1016/j.chemgeo.2008.12.005. Woodall, C. M.; McQueen, N.; Wilcox, J. Carbon mineralization using plagioclase feldspar-rich mine tailings: characterization and cation extraction. 2021, pp 15-18. Berrezueta, E.; Moita, P.; Pedro, J.; Abdoulghafour, H.; Mirão, J.; Beltrame, M.; Barrulas, P.; Araújo, A.; Caeiro, M. H.; Luis, L. Laboratory experiments and modelling of the geochemical interaction of a gabbro-anorthosite with seawater and supercritical CO2: A mineral carbonation study. *Geoenergy Science and Engineering* **2023**, 212010. Lin, H.; Fujii, T.; Takisawa, R.; Takahashi, T.; Hashida, T. Experimental evaluation of interactions in supercritical CO_2/water/rock minerals system under geologic CO_2 sequestration conditions. *Journal of Materials Science* **2008**, *43* (7), 2307-2315. DOI: 10.1007/s10853-007-2029-4. Sugama, T.; Ecker, L.; Butcher, T. Carbonation of rock minerals by supercritical carbon dioxide at 250°C. Division, E. R. D. E. R., Ed.; Brookhaven National Laboratory: Upton, NY, 2010.

(26) Hamilton, J. L.; Wilson, S.; Morgan, B.; Turvey, C. C.; Paterson, D. J.; Jowitt, S. M.; McCutcheon, J.; Southam, G. Fate of transition metals during passive carbonation of ultramafic mine tailings via air capture with potential for metal resource recovery. *International Journal of Greenhouse Gas Control* **2018**, *71*, 155-167. Hamilton, J. L.; Wilson, S.; Morgan, B.; Harrison, A. L.; Turvey, C. C.; Paterson, D. J.; Dipple, G. M.; Southam, G. Accelerating mineral carbonation in ultramafic mine tailings via direct CO2 reaction and heap leaching with potential for base metal enrichment and recovery. *Economic Geology* **2020**, *115* (2), 303-323. Honda-McNeil, M. J. A Geometallurgical Approach to Assessing Critical Metal Mobility and Recoverability from Ultramafic Mine Tailings. **2022**.

(27) Wang, F.; Dreisinger, D. An integrated process of CO2 mineralization and selective nickel and cobalt recovery from olivine and laterites. *Chemical Engineering Journal* **2023**, *451*, 139002. DOI: https://doi.org/10.1016/j.cej.2022.139002. Wang, F.; Dreisinger, D. Carbon mineralization with concurrent critical metal recovery from olivine. *Proc. Natl. Acad. Sci. U.S.A.* **2022**, *119* (32), e2203937119.

(28) Wang, F.; Dreisinger, D. Enhanced CO2 mineralization and selective critical metal extraction from olivine and laterites. *Separation and Purification Technology* **2023**, 124268.

(29) Peck, D. C.; Huminicki, M. A. E. Value of mineral deposits associated with mafic and ultramafic magmatism: Implications for exploration strategies. *Ore Geology Reviews* **2016**, *72*, 269-298. DOI: https://doi.org/10.1016/j.oregeorev.2015.06.004.

(30) Naldrett, A. J.; Cabri, L. J. Ultramafic and related mafic rocks; their classification and genesis with special reference to the concentration of nickel sulfides and platinum-group elements. *Economic Geology* **1976**, *71* (7), 1131-1158. Smith, J. M.; Ripley, E. M.; Li, C.; Shirey, S. B.; Benson, E. K. Magmatic origin for the massive sulfide ores in the sedimentary country rocks of mafic–ultramafic intrusions in the Midcontinent Rift System. *Mineralium Deposita* **2022**, *57* (7), 1189-1210. DOI: 10.1007/s00126-022-01095-2.

(31) *The role of critical minerals in clean energy transitions*; International Energy Agency, 2021.

(32) Hund, K. L.; Arrobas, D. L. P.; Fabregas Masllovet, T. P.; Laing, T. J.; Drexhage, J. R. Minerals for climate action: The mineral intensity of the clean energy transition. **2023**.

(33) Morfin, A. M.; Stanfield, C. H.; Murchland, M. A.; Bartels, M. F.; Nagurney, A. B.; Miller, Q. R. S.; Schaef, H. T. Structure–Composition Relationships for Mg–Ni and Mg–Fe Olivine. *ACS Earth Space Chem.* **2024**, *8* (9), 1713-1724. Ghaderi, S.; Ji, B.; Michael Veach, D.; Alissa Park, A.-H.; Meng, J.; Zhang, W. A comprehensive study on the leaching characteristics and mechanisms of nickel and cobalt from olivine. *Minerals Engineering* **2024**, *218*, 108992. DOI: https://doi.org/10.1016/j.mineng.2024.108992. Barnes, S. J.; Yao, Z.-S.; Mao, Y.-J.; Jesus, A. P.; Yang, S.; Taranovic, V.; Maier, W. D. Nickel in olivine as an exploration indicator for magmatic Ni-Cu sulfide deposits: A data review and re-evaluation. *American Mineralogist* **2023**, *108* (1), 1-17. DOI: 10.2138/am-2022-8327.

(34) Hamilton, J. L.; Wilson, S. A.; Morgan, B.; Harrison, A. L.; Turvey, C. C.; Paterson, D. J.; Dipple, G. M.; Southam, G. Accelerating mineral carbonation in ultramafic mine tailings via direct CO_2 reaction and heap leaching with potential for base metal enrichment and recovery. *Economic Geology* **2020**, *115* (2), 303-323. Wilson, S.; Hamilton, J. L. Fizzy ore processing sequesters CO_2 while supplying critical metals. *Proceedings of the National Academy of Sciences* **2022**, *119* (39), e2212424119. DOI: doi:10.1073/pnas.2212424119. Wang, F.; Dreisinger, D. Carbon mineralization with concurrent critical metal recovery from olivine. **2022**, *119* (32), e2203937119. DOI: doi:10.1073/pnas.2203937119. Wang, F.; Dreisinger, D. Enhanced CO2 mineralization and selective critical metal extraction from olivine and laterites. *Separation and Purification Technology* **2023**, *321*, 124268. DOI: https://doi.org/10.1016/j.seppur.2023.124268. Wang, F.; Dreisinger, D.; Xiao, Y. Accelerated CO2 mineralization and utilization for selective battery metals recovery from olivine and laterites. *Journal of Cleaner Production* **2023**, *393*, 136345. DOI:

https://doi.org/10.1016/j.jclepro.2023.136345. Murchland, M. A.; Nagurney, A. B.; Lahiri, N.; Engelhard, M. H.; Schaef, H. T.; Miller, Q. R. S. V23B-0164: Concurrent Carbon Mineralization and Critical Metal Mobilization in Eagle Intrusion Peridotites. In AGU Annual Fall Meeting 2023, San Francisco, California; Paper V23B-0164, 2023. Wang, F.; Dreisinger, D.; Barr, G. Accelerated CO2 Mineralization and Simultaneous Critical Metal Recovery from Ultramafic Tailings. In *Proceedings of the 62nd Conference of Metallurgists, COM 2023*, Cham, 2023//, 2023; Springer Nature Switzerland: pp 45-53. Zhang, N.; Yang, R.; Huang, H. D.; Meng, J.; Zhang, W.; Park, A.-H. A.; Moment, A. Integrated Recovery of Iron and Nickel from Olivine Ores Using Solvent Extraction: Synergistic Production of Amorphous Silica and Carbonates through pH Adjustment and Carbon Mineralization. *ACS ES&T Engineering* **2024**. DOI: 10.1021/acsestengg.4c00462. Gazzetti, E. W.; Bandstra, J. Z.; Diedrich, T. R. Valorisation of mine waste as carbon mineralisation feedstock. In Mine Closure 2023: Proceedings of the 16th International Conference on Mine Closure, Reno; 2023. Wang, B.; Zeyen, N.; Wilson, S.; Honda-McNeil, M. J.; Hamilton, J. L.; Von Gunten, K.; Alessi, D. S.; Jones, T. R.; Paterson, D. J.; Southam, G. Migration of transition metals and potential for carbon mineralization during acid leaching of processed kimberlite from Venetia diamond mine, South Africa. *Applied Geochemistry* **2024**, *166*, 105986. DOI: https://doi.org/10.1016/j.apgeochem.2024.105986. Wilson, S.; Turvey, C.; Hamilton, J. L.; Power, I. M.; Hussain, A. Critical Metals and the Need for Low CO 2 Mining Poster. In *AGU23*, 2023; AGU. Katre, S.; Ochonma, P.; Asgar, H.; Nair, A. M.; Ravi, K.; Gadikota, G. Mechanistic insights into the co-recovery of nickel and iron via integrated carbon mineralization of serpentinized peridotite by harnessing organic ligands. *Physical Chemistry Chemical Physics* **2024**, *26* (12), 9264-9283. Honda-McNeil, M. J. A Geometallurgical Approach to Assessing Critical Metal Mobility and Recoverability from Ultramafic Mine Tailings. University of Alberta, 2022. Hamilton, J. L.; Wilson, S. A.; Morgan, B.; Turvey, C. C.; Paterson, D. J.; Jowitt, S. M.; McCutcheon, J.; Southam, G. Fate of transition metals during passive carbonation of ultramafic mine tailings via air capture with potential for metal resource recovery. *International Journal of Greenhouse Gas Control* **2018**, *71*, 155-167. DOI: 10.1016/j.ijggc.2018.02.008. Wicks, D.; King, J. Sequestering Carbon with Hybrid Employment of Mineral Assets. In *CO2 Mineralization for in situ Storage and ex situ Enhanced Metals Recovery Workshop*, 2021. Gao, Y.; Jin, X.; Teng, L.; Rohani, S.; He, M.; Li, J.; Ren, S.; Liu, Q.; Huang, J.; Duan, H.; et al. CO2 mineral sequestration and nickel recovery from laterite ore by using waste copperas. *Fuel* **2023**, *331*, 125750. DOI: https://doi.org/10.1016/j.fuel.2022.125750. Miller, Q. R.; Nagurney, A.; Blondes, M.; Thakurta, J.; Liu, J.; Gadikota, G.; Lahiri, N.; Schaef, H. T. Carbon-negative nickel mining to meet global mineral resource demands. **2025**. DOI: https://doi.org/10.31223/X5S15S.

(35) Santos, R. M.; Van Audenaerde, A.; Chiang, Y. W.; Iacobescu, R. I.; Knops, P.; Van Gerven, T. Nickel Extraction from Olivine: Effect of Carbonation Pre-Treatment. *Metals* **2015**, *5* (3), 1620-1644. DOI: 10.3390/met5031620.

(36) Jacobs, J. E.; Stanfield, C. H.; Miller, Q. R. S.; Villante, M. A.; Marcial, J.; Nienhuis, E. T.; Silverstein, J. A.; Polites, E. G.; Bartels, M. F.; Gooch, B. T.; et al. Technoeconomic Potential for Carbon Mineralization with Enhanced Recovery of Critical Minerals in the Pacific Northwest. *ACS Sustainable Resource Management* **2025**, *2* (5), 775-785. DOI: 10.1021/acssusresmgt.4c00541.

(37) Ripley, E. M.; Li, C. A review of conduit-related Ni-Cu-(PGE) sulfide mineralization at the Voisey's Bay deposit, Labrador, and the Eagle deposit, northern Michigan. *Reviews in Economic Geology* **2011**, *17*. Ding, X.; Ripley, E. M.; Li, C. PGE geochemistry of the Eagle Ni–Cu–(PGE) deposit, Upper Michigan: constraints on ore genesis in a dynamic magma conduit. *Mineralium Deposita* **2012**, *47*, 89-104. Ripley, E. M. Ni-Cu-PGE mineralization in the Partridge River, South Kawishiwi, and Eagle intrusions: a review of contrasting styles of sulfide-rich occurrences in the Midcontinent Rift System. *Economic Geology* **2014**, *109* (2), 309-324. Hinks, B. D. Geochemical and petrological studies on the origin of nickel-copper sulfide mineralization at the Eagle lntrusion in Marquette County, Michigan. Western Minchigan University, 2016.

(38) Mulcahy, C. Emplacement and crystallization hstories of Cu-Ni-PGE sulfide-mineralized peridotites in the Eagle and Eagle East intrusions. University of Minnesota, 2018.

(39) Ding, X.; Li, C.; Ripley, E. M.; Rossell, D.; Kamo, S. The Eagle and East Eagle sulfide ore-bearing mafic-ultramafic intrusions in the Midcontinent Rift System, upper Michigan: Geochronology and petrologic evolution. *Geochemistry, Geophysics, Geosystems* **2010**, *11* (3). DOI: https://doi.org/10.1029/2009GC002546.

(40) Loughran, R. P.; Hurley, T.; Gładysiak, A.; Chidambaram, A.; Khivantsev, K.; Walter, E. D.; Graham, T. R.; Reardon, P.; Szanyi, J.; Fast, D. B.; et al. CO_2 capture from wet flue gas using a water-stable and cost-effective metal-organic framework. *Cell Rep. Phys. Sci* **2023**, *4* (7), 101470. DOI: https://doi.org/10.1016/j.xcrp.2023.101470. Haider, M. M.; Jian, G.; Li, H.; Wolcott, M.; Fernandez, C.; Miller, Q. R. S.; Nassiri, S. Impact of chitin nanofibers and nanocrystals from waste shrimp shells on mechanical properties, setting time, and late-age hydration of mortar. *Sci. Rep.* **2022**, *12* (1), 20539. DOI: 10.1038/s41598-022-24366-4 From NLM. Strange, L. E.; Shutthanandan, V.; Song, M.; Bowden, M.; Miller, Q. R. S.; Prabhakaran, R.; Shimskey, R.; Joshi, V. V. Multimodal analysis and characterization of the boehmite layer formed on AA6061 before and after alkaline etching. *Journal of Materials Research and Technology* **2022**, *21*, 1274-1281. DOI: 10.1016/j.jmrt.2022.09.125. Bartels, M. F.; Miller, Q. R. S.; Cao, R.; Lahiri, N.; Holliman, J. E., Jr.; Stanfield, C. H.; Schaef, H. T. Parts-Per-Million Carbonate Mineral Quantification with Thermogravimetric Analysis–Mass Spectrometry. *Analytical Chemistry* **2024**, *96* (11), 4385-4393. DOI: 10.1021/acs.analchem.3c03936. Zhou, J.; Holekevi Chandrappa, M. L.; Tan, S.; Wang, S.; Wu, C.; Nguyen, H.; Wang, C.; Liu, H.; Yu, S.; Miller, Q. R. S.; et al. Healable and conductive sulfur iodide for solid-state Li–S batteries. *Nature* **2024**, *627* (8003), 301-305. DOI: 10.1038/s41586-024-07101-z.

(41) Aguila, B.; Hardee, L.; Schaef, H. T.; Zare, S.; Qomi, M. J. A.; Crum, J. V.; Holliman Jr, J. E.; Rodriguez, E. T.; Anovitz, L. M.; Rosso, K. M. Emerging investigator series: kinetics of diopside reactivity for carbon mineralization in mafic–ultramafic rocks. *Environmental Science: Nano* **2023**, *10* (10), 2672-2684.
(42) Depp, C. T.; Miller, Q. R. S.; Crum, J. V.; Horner, J. A.; Schaef, H. T. Pore-Scale Microenvironments Control Anthropogenic Carbon Mineralization Outcomes in Basalt. *ACS Earth and Space Chemistry* **2022**, *6* (12), 2836-2847.
(43) Davis, K. J.; Dove, P. M.; De Yoreo, J. J. The role of Mg2+ as an impurity in calcite growth. *Science* **2000**, *290* (5494), 1134-1137. Reddy, M. M.; Wang, K. K. Crystallization of calcium carbonate in the presence of metal ions: I. Inhibition by magnesium ion at pH 8.8 and 25 C. *Journal of Crystal Growth* **1980**, *50* (2), 470-480. Berner, R. A. The role of magnesium in the crystal growth of calcite and aragonite from sea water. *Geochimica et Cosmochimica Acta* **1975**, *39* (4), 489-504.
(44) Ding, X.; Li, C.; Ripley, E. M.; Rossell, D.; Kamo, S. The Eagle and East Eagle sulfide ore-bearing mafic-ultramafic intrusions in the Midcontinent Rift system, upper Michigan: Geochronology and petrologic evolution. *Geochemistry, Geophysics, Geosystems* **2010**, *11* (3).
(45) *Nickel*. Trading Economics, 2023. https://tradingeconomics.com/commodity/nickel (accessed 07/20/2023).
(46) Hodgkinson, J. H.; Smith, M. H. Climate change and sustainability as drivers for the next mining and metals boom: The need for climate-smart mining and recycling. *Resources Policy* **2021**, *74*, 101205.
(47) Delevingne, L.; Glazener, W.; Grégoir, L.; Henderson, K. Climate risk and decarbonization: What every mining CEO needs to know. *McKinsey Insights* **2020**.

Supporting Information

CO_2-Based Leaching of Peridotite Drives Critical Mineral Mobilization and Carbonate Precipitation

Madeline A. Murchland [a†*], Quin R.S. Miller [a*], C. Heath Stanfield [a], Alexandra B. Nagurney [a], Nabajit Lahiri [a], Joshua A. Silverstein [a], Yuntian Teng [a], Emily T. Nienhuis [b], Mark H. Engelhard [a], Connor C. Mulcahy [c], H. Todd Schaef [a]

[a] Energy and Environment Directorate, Pacific Northwest National Laboratory, Richland, Washington, USA
[b] Physical and Computational Sciences Directorate, Pacific Northwest National Laboratory, Richland, Washington, USA
[c] Division of Environmental Management, Wisconsin Department of Natural Resources, Milwaukee, Wisconsin, USA
[†] Current affiliation is Department of Geology and Geological Engineering, Colorado School of Mines, Golden, Colorado, USA

10 Pages
5 Figures
3 Tables

[*]Corresponding authors contact information:
madeline_murchland@mines.edu, quin.miller@pnnl.gov

METHODS

X-Ray Microtomography (XMT). In this study, we adopted high-resolution X-ray microtomography (XMT) technology and image analysis on the reacted sample. The XMT scanning of reacted sample was conducted with Bruker's Skyscan 1273, with a pixel resolution of 8 μm. The energy level was at 130 kV and 57 μA and two radiographies were collected every 0.3° of a 360° rotation. After the XMT scanning, we reconstructed the three-dimensional model of the entire sample using the Bruker NReconn software package. Then, we applied Avizo 3D software and Dragonfly 3D software for image processing, segmentation, and extraction of the geometrical information of the sample. The reconstructed digital surface of the reacted sample is shown in Figure S5a. Further analysis focused on the center portion shown in Figure S5b, to match the μXRF analytical region. Three phases of material were segmented and labeled in Figure S5c based on the intensity histogram. Yellow areas represent highest density material, sulfide. Green areas are pyroxene and the remaining material represents the less dense silicate phases, olivine and plagioclase.

Three-dimensional reconstructed model also provided geometrical data of this reacted sample. The total volume is 508.31 mm^3, 8.77% of which is sulfide, which is 44.60 mm^3.

FIGURES

Figure S1: Flow chart depicting the process of examining, carbonating, and re-examining the peridotite chip via multimodal characterization techniques including micro-XRF (µXRF), scanning electron microscopy with energy dispersive spectroscopy (SEM-EDS), X-ray photoelectron spectroscopy (XPS), micro-XRD (µXRD), advanced mineral analysis and characterization system (AMICS), and X-ray microtomography. The process contributed towards method development for similar future experiments.

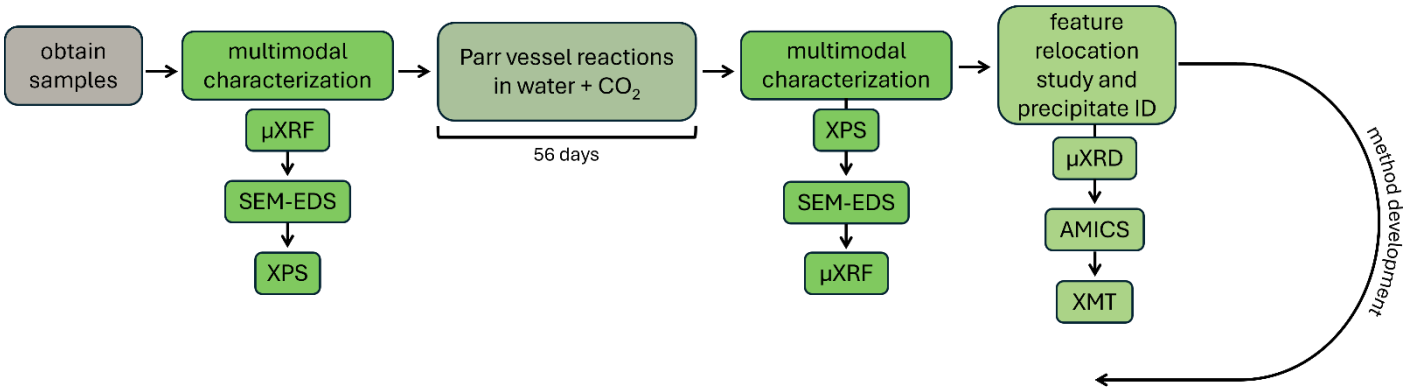

Figure S2: Schematic showing the portion of sample probed with each method and relative excitation volume of the corresponding analysis (not to scale).

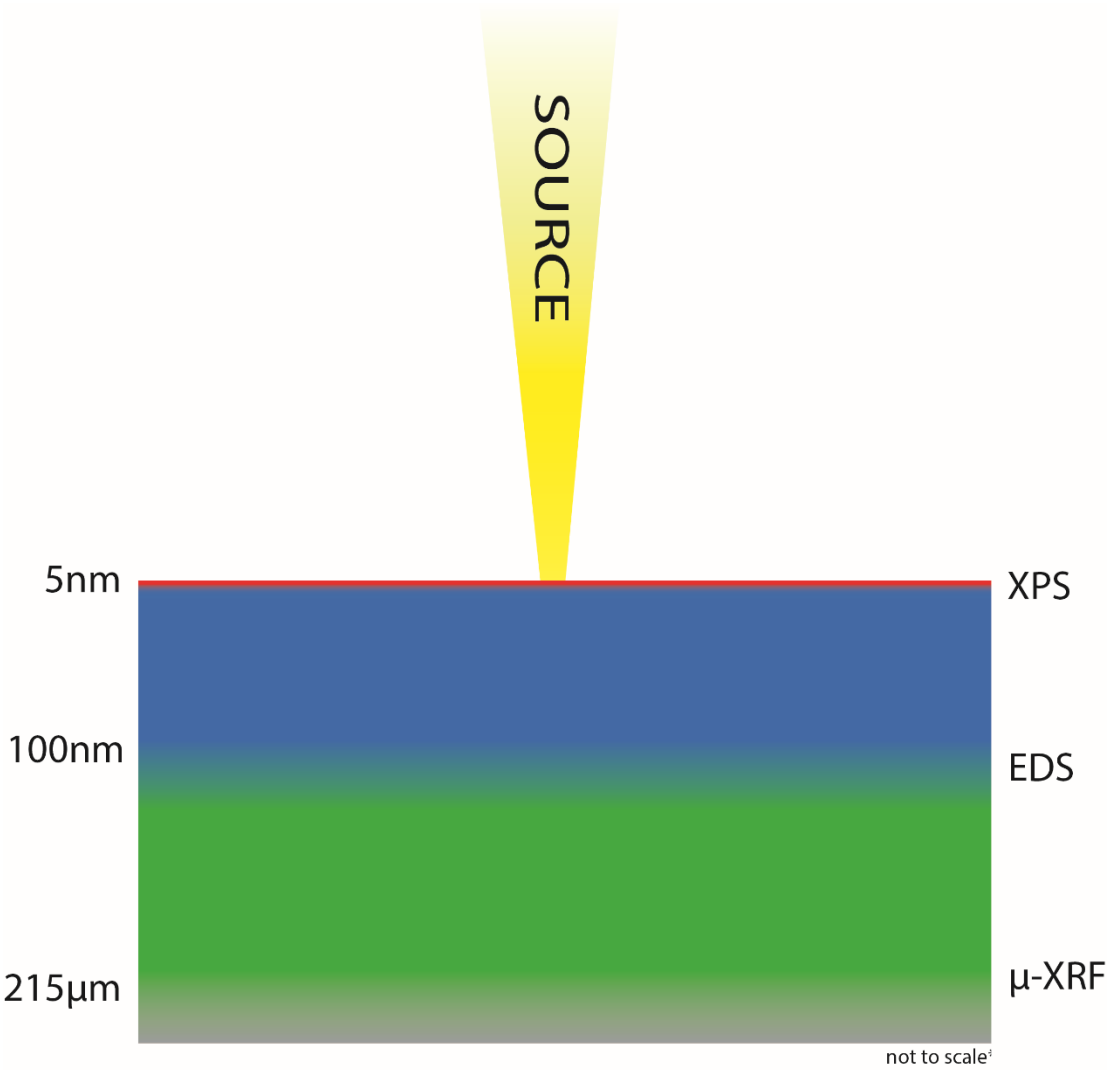

Figure S3: Optical photos of the Eagle Mine peridotite chip. (a) Unreacted rock chip. Green area represents the portion of chip analyzed with µXRF. (b) Reacted rock chip.

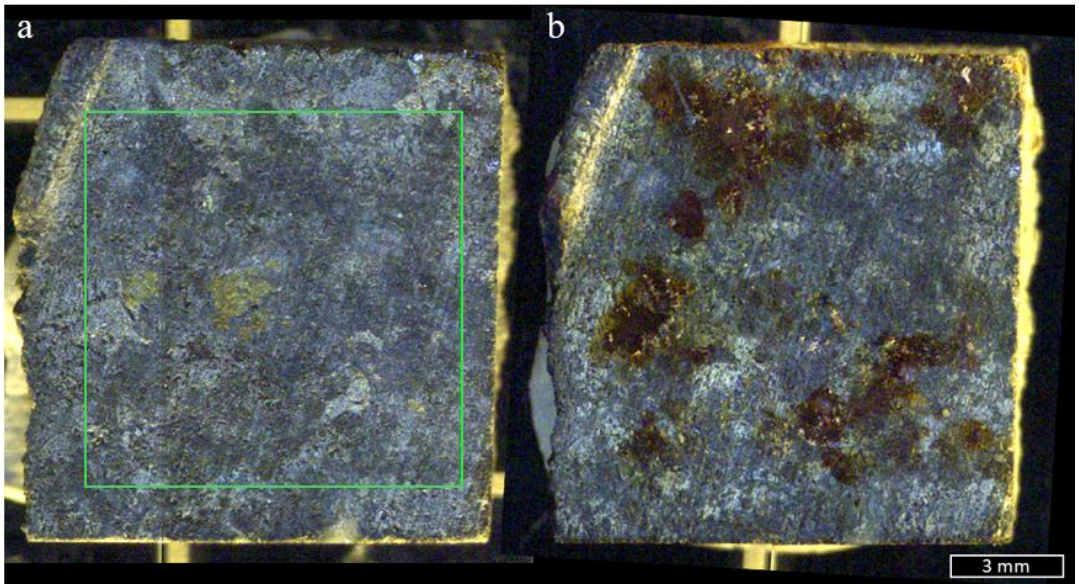

Figure S4: a) Digital microscopy image of the post-reaction chip probed by micro XRD to determine mineralogy of Fe-rich and Mg- and Si-deficient feature that covers up a portion of olivine in the unreacted rock. digital optical microscopy image. b) Two-dimensional detector image showing diffraction rings and spots. c) Integration of the detector image to produce a diffractogram reveals the presence of peaks corresponding to hematite (Fe_2O_3). The peak locations match with the International Centre for Diffraction Data powder diffraction file (PDF) entry for hematite; PDF# 00-006-0502.

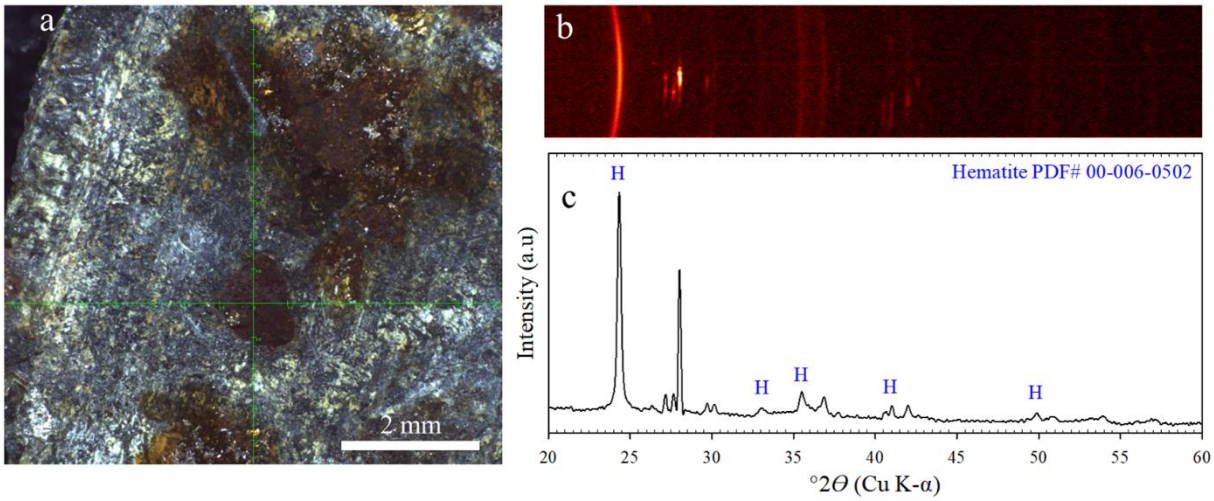

Figure S5: a) Reconstructed digital surface of reacted sample resulting from XMT analysis. Analytical area marked in green. b) Reconstructed digital surface of the analytical area b) Mineral phases segmented based on intensity histogram. Yellow areas represent sulfides, the highest density material in the chip. Green areas are pyroxene, and the rest represents the other less dense silicates, olivine and plagioclase.

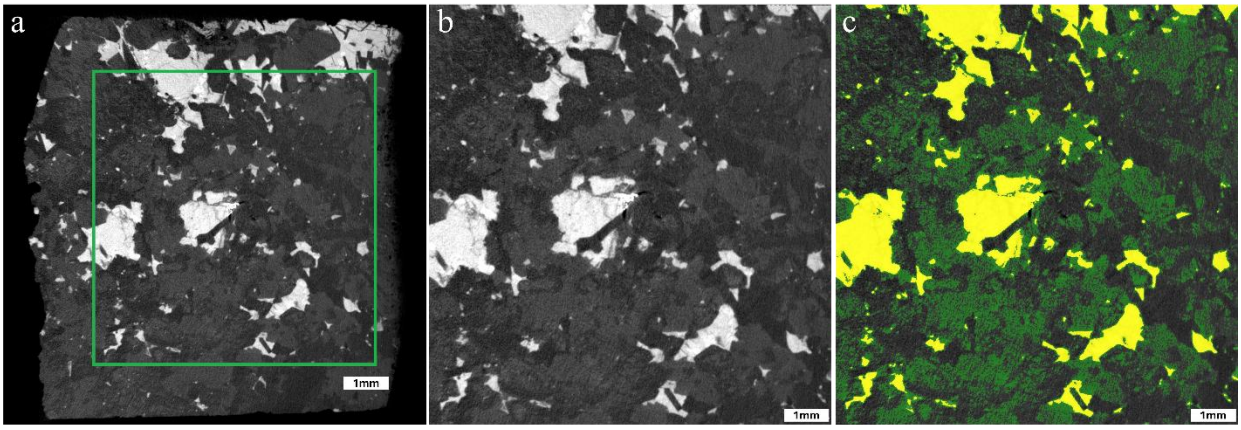

TABLES

Table S1: Wt% and area % of mineral phases for both the unreacted and reacted sample, based on µXRF results analyzed with AMICS

	Unreacted Sample		**Reacted Sample**	
Mineral Phase	**Wt%**	**Area %**	**Wt%**	**Area %**
olivine	35.86	38.60	29.94	32.63
augite	31.39	32.08	30.64	32.87
plagioclase	6.15	8.01	5.61	7.45
diopside	0.58	0.61	0.51	0.54
titano-magnetite	0.65	0.72	0.55	0.61
carbonate	0.29	0.38	0.83	1.10
pyrrhotite	7.74	5.63	3.75	2.95
pentlandite	1.25	0.93	2.54	1.92
violarite	4.43	3.40	7.50	5.84
chalcopyrite	5.89	5.01	5.73	4.94
ilmenite	1.59	1.20	1.27	0.97
chromite	1.21	0.90	1.16	0.87
hematite	2.50	1.69	9.50	6.49
unknown	0.47	0.84	0.41	0.74

Table S2: Oxide composition (wt%) from µXRF for the bulk sample, olivine (3200 ppm Ni), plagioclase feldspar, pyroxene, and sulfide.

Oxide	Composition (oxide wt%)				
	Bulk	**Olivine** Fo80 (forsteritic olivine)	**Plagioclase** An70 (labradorite)	**Pyroxene** Wo29En54Fs17 (augite)	**Sulfide**
SiO_2	37.50	38.57	48.38	48.31	6.30
TiO_2	0.69	0.64	0.26	0.53	0.16
Al_2O_3	5.02	3.55	23.91	9.25	1.03
CaO	5.11	2.63	7.99	11.61	1.28
Fe_2O_3	19.47	21.63	6.85	10.28	31.62
MgO	22.08	27.95	6.21	16.45	4.84
MnO	0.23	0.25	0.23	0.22	0.03
K_2O	0.29	0.28	1.02	0.39	0.05
Na_2O	0.87	0.89	3.88	1.55	0.45
NiO	0.47	0.41	0.04	0.07	2.57
Cu_2O	0.54	0.24	0.09	-	4.87
Cr_2O_3	0.38	0.31	-	0.52	-
SO_3	7.35	2.65	1.15	0.83	46.78

Table S3: Normalized elemental composition (wt%) from µXRF for the bulk sulfidic peridotite sample, along with the sulfide compositions for pyrrhotite, chalcopyrite, and pentlandite.

Element	Composition* (normalized elemental wt%)			
	Bulk	**Pyrrhotite** $Fe_{1-x}S$ (Fe_7S_8 to Fe_9S_{10})	**Chalcopyrite** $CuFeS_2$	**Pentlandite** $(Fe,Ni)_9S_8$
S	2.94	36.27	31.55	28.76
Fe	13.62	59.76	30.16	33.82
Mg	13.31	1.40	2.14	4.40
Si	17.53	1.54	2.53	3.62
Al	2.66	0.31	0.53	0.32
Ca	3.65	0.19	0.70	1.28
Ni	0.37	0.22	0.08	27.54
Na	0.64	0.08	1.51	-
Cu	0.49	0.17	30.65	0.17
K	0.24	0.03	0.03	0.01
Ti	0.41	0.03	0.04	0.08
O*	43.64	-	-	-
Mn	0.18	-	0.08	0.01
Cr	0.26	-	-	-
Cl	0.06	-	-	-

* Oxygen abundance is calculated, not directly measured